ROYAL INSTITUTE
OF TECHNOLOGY

Narrow Linewidth All-fiber Cavity Thulium Fiber Laser at 2 μm

ROBERT W. HURRA
HURRA@KTH.SE

Degree in Engineering Physics, SK200X
Royal Institute of Technology
Department of Laser Physics

Supervisor:
Fredrik Laurell

Examinator:
Valdas Pasiskevicius

TRITA-FYS 2014:17 ISSN 0280-316X ISRN KTH/FYS/--14:17–SE

Abstract

The aim of this project is to develop a stable, narrow linewidth, all-fiber cavity thulium fiber laser with an output wavelength around 2 μm. There are several important fields of applications for a narrow linewidth laser, including the area of optical sensors, spectroscopy and for optical fiber communication. A narrow linewidth can be obtained with wavelength selecting elements such as fiber Bragg gratings, volume Bragg gratings, diffraction gratings and intra-cavity etalons. However, an all-fiber cavity was desired and, therefore, fiber Bragg gratings were the element of choice. An all-fiber cavity is robust, compact, cheap and alignment free.

The rare-earth element thulium has a broad gain-bandwidth allowing ultrashort pulse operation, and a wide wavelength tunability. Thulium has emission peaks located at eye-safe wavelengths, which open up applications within the field of medicine, spanning 400 nm, ranging from 1700 to 2100 nm. Therefore, thulium fiber lasers provide the possibility of amplification windows other than the currently established window around 1550 nm, using erbium amplifiers. The output of the thulium fiber laser could, in turn, be used as a pump source for non-linear frequency conversion schemes extending the output wavelength to the 3-10 μm range.

High-power fiber lasers commonly rely on master oscillator power amplification schemes, which makes a robust and compact seed source with excellent spectral and spatial beam quality desirable, which an all-fiber cavity laser provides. During this thesis work, such a source was realized, by developing a cladding-pumped fiber Bragg grating-locked thulium all-fiber cavity laser.

The thulium fiber laser was characterized by investigating the threshold input and maximum output power, which were 1.12 W and 0.86 W, respectively. The slope efficiency was found to be 47%, with respect to the absorbed pump power, with very good spatial beam quality, $M^2 \leq 1.05$. Analyzing the spectral beam quality showed a central wavelength of 2051 nm, with a full width at half maximum of 1.5 nm. The characteristics were also investigated with the coiling diameter of the active thulium fiber as a variable.

Acknowledgements

I want to thank the Department of Laser Physics at the Royal Institute of Technology for offering me a very interesting and challenging master thesis project. I would especially like to express my gratitude to my supervisor **Professor Fredrik Laurell** and my examinator **Professor Valdas Pasiskevicius** who helped me throughout this thesis.

All the staff at Laser Physics, including **Hoda Kianirad**, **Mikael Malmström**, **Riaan S. Coetzee**, **Michael Fokine**, **Patrick Holmberg**, **Nicky Thilmann**, **Zangwei Yu** and others deserve credits for their expertise and for providing a friendly and social study environment. I particularly want to thank **Peter Zeil**, who spent a lot of time with me, both in the lab and proof-reading my thesis.

My fellow master students, **Pavel Delgado-Goroun**, **Robert Enrico Lindberg** and **Petter Andersson**, for talking non-sense and playing cards with me from time to time.

My parents **Solveig** and **Rainer Hurra** for giving me shelter and food, and for trying to understand when I talk physics with them.

My friends **Brallan** and **D-Pain** for crazy nights out.

To **all my friends** which were not mentioned, but never forgotten.

And finally **Jovana Ćirjaković** for being the girl in my life ♡

Contents

List of Figures

List of Tables

Abbreviations

AFM	atomic force microscopy
Al	aluminium
AR	anti-reflection
ASE	amplified spontaneous emission
CMT	coupled-mode theory
CR	cross-relaxation
CW	continuous wave
DC	double-clad
DIRCM	directional infrared counter measures
Er	erbium
FBG	fiber Bragg grating
FWHM	full width at half maximum
H	hydrogen
HeNe	helium-neon
Ho	holmium
HR	highly reflective
HT	highly transmittive
IR	infrared

LD	laser diode
MOFA	master oscillator fiber amplifier
MOPA	master oscillator power amplifier
NA	numerical aperture
NIR	near-infrared
non-PM	non-polarization maintaining
PbP	point-by-point
PER	polarization extinction ratio
RE	rare-earth
SBS	stimulated Brillouin scattering
Si	silica
SM	single-mode
SPM	self-phase modulation
SRS	stimulated Raman scattering
TEM	transmission electron microscopy
TFL	thulium fiber laser
TIR	total internal reflection
Tm	thulium
UV	ultraviolet
XPM	cross-phase modulation
Yb	ytterbium

Nomenclature

I_{LD}	Laser diode pump current
I_{th}	Laser diode threshold current
M^2	Beam propagation factor
P_{max}	Maximum power
P_{th}	Power threshold
R_{NTC}	Resistance of NTC thermistor
Γ	Overlap coefficient
δ	Detuning wave vector
η_{CR}	Cross-relaxation efficiency
η_{s}	Slope efficiency
$\hat{\sigma}$	General DC self-coupling coefficient
κ	AC coupling coefficient
λ_{D}	Design wavelength
ϕ	Coiling diameter of the active fiber
σ_{12}	Absorption cross-section
σ_{21}	Emission cross-section
θ	Half-angle beam divergence
$\tilde{f}$	Focusing power of lens surface
υ_{A}	Acoustic velocity
υ_{B}	Brillouin frequency
$\varphi(z)$	Grating chirp
f	Focal length of a lens
r_{cl}	Radius of the fiber cladding
r_{max}	Maximum reflectivity of a FBG
r_{r}	Repetition rate

v_{s}	Scanning velocity
D_{L}	Beam diameter at $\frac{1}{e}$ of maximum irradiance
E_0	Irradiance at the center of a Gaussian beam
J_0	First root of the Bessel function
P_{p}	Pump power
V_{nr}	V-number, normalized frequency number
Λ	Grating period of a FBG
Φ_0	Total power in a Gaussian beam
β	Propagation constant
λ	Optical wavelength
λ_{p}	Pump wavelength
ω	Beam radius
ω_0	Beam waist radius
n	Refractive index of a medium
n_{eff}	Effective refractive index
q	Complex beam parameter
r_{c}	Radius of the fiber core
v	Fringe visibility of the index change (in a FBG)
z_{R}	Rayleigh range

Chapter 1

Introduction

1.1 Fiber lasers

Since the early days of fiber optics, when Charles K. Kao first proposed that the high losses of optical fibers were due to impurities in the glass rather than the technology itself in 1965 [1], the technology has come a long way. The technology has gone from losses of many dB/m to losses below 1 dB/km, and is used in a vast amount of applications - mainly within the fields of communication and sensors.

When optical fibers became the major component in the field of communication in the 1980s, deteriorated optical signals needed reamplifying due to long transmission lines. The first fiber amplifiers, pioneered by David N. Payne in the late 1980's [2], were doped with the rare-earth (RE) element erbium (Er). This concept of doping active ions in optical fibers eventually matured which led to fiber lasers being the frontier in high-power laser development. Fiber lasers are often called or referred to as brightness converters, since they convert a low brightness pump source with a high beam quality factor, into a high brightness output with low beam quality factor. Fibers doped with RE elements provide strong amplification and are by far the most common gain medium in fiber lasers.

The RE ytterbium (Yb) has great power-scaling properties due to its low quantum defect and high pump absorption per unit length [3], and Yb-doped fiber lasers are, to this day, still the record-holder in terms of power scaling and laser performance with up to 10 kW in the single-mode (SM) regime in continuous wave (CW) operation [4]. On the other hand, Yb has en emission around 1 μm, and is thus limited to only

a few applications. Therefore there is an increased interest in other RE elements such as thulium (Tm) and holmium (Ho), in order to realize high-power sources in the 2 μm range. Jackson managed to obtain a slope efficiency of 75%, which is the highest recorded slope efficiency in a thulium fiber laser (TFL) to date [5]. Jackson's setup was although not an all-fiber cavity. The best slope efficiency for an all-fiber cavity was developed at Shanghai Jiaotong University by Tang *et al* with a slope efficiency of 62% [6]. The highest output power to date for a TFL is above 1 kW, with a slope efficiency of ~53%, obtained with a master oscillator power amplifier (MOPA) scheme and two Tm fiber power amplification stages, developed by Ehrenreich *et al* [7].

The aim of this thesis is to develop a narrowband Tm source, with an all-fiber cavity. Tm has retina safe emission peaks, of a span of 400 nm, ranging from 1.7 μm up to 2.1 μm, which are of particular interest for a range of applications, mainly within the fields of communication, sensoring and medicine. If the TFL is used as a pump source for non-linear frequency conversion schemes, targeting the 3-10 μm region, applications within spectroscopy is available. Spectral beam combining is yet another application which has led to high power levels unattainable from conventional single fiber laser sources [6], and if the source successfully manages to lase at a single-frequency, the possibility of coherent beam combining opens up. The list of applications can be long, a few other applications are e.g. LIDAR [8] or using the TFL as a pump source for Ho, which gives even longer wavelengths and thus enables further applications such as directional infrared counter measures (DIRCM) [9].

1.2 Structure of the thesis

This thesis will first introduce some basic theory regarding fiber optics, including light propagation in optical fibers, Gaussian beams, and different pumping schemes. Spectral properties of the RE Tm are thereafter discussed in the chapter "Narrowband Thulium Fiber Lasers" followed by a theoretical study of the fiber Bragg grating (FBG). The physical system was modelled, and the approach to obtain accurate simulations are explained.

The experimental setup, and the all-fiber cavity is explained in detail, followed by how the fiber parameters were chosen in order to create a cladding-pumped

scheme. The final setup to characterize the output signal is finally discussed. After the experimental setups have been introduced, the experimental results are presented, including power measurements, laser polarization, spectral and spatial characterization.

The thesis is then finally concluded with a discussion followed by conclusions, suggested improvements, and future work.

Chapter 2

Fiber Lasers

The fiber laser has several advantages over a traditional solid-state laser. The most obvious advantage of an all-fiber laser is the lack of alignment of free-space components. The systems are considered to be robust and compact due to possible all-fiber setups and the use of fiber yields excellent heat removal. In contrast to crystal-based solid-state lasers, excess heat will be efficiently dissipated in fiber lasers, due to their large surface area to volume ratio. The fiber has excellent beam quality, since the fiber is a waveguide, and the long interaction length provide high gain systems, offering the option of master oscillator fiber amplifier (MOFA) schemes [3]. Most fibers are fabricated in silica (Si), and since the glass host is of amorphous structure that broadens the laser transitions in the RE dopants, fiber lasers have a broad gain-bandwidth. This allows the laser to operate with a broad spectrum, which, with the modes in the spectrum phase-locked with respect to each other, supports ultrashort pulse operation.

This chapter will introduce relevant theory to explain the above claims. First of all, will waveguiding in optical fibers be treated, and non-linear propagation effects, e.g. self-phase modulation (SPM), stimulated Raman scattering (SRS), and stimulated Brillouin scattering (SBS). However, these non-linear effects are very weak in the developed system, and can therefore be neglected. The next section will describe possible pumping schemes, and how to physically launch pump power into an optical fiber.

2.1 Light propagation in optical fibers

2.1.1 Waveguiding in optical fibers

The most common waveguiding property in fiber optics is total internal reflection (TIR), but there are though fibers which guide light without the use of TIR, called photonic crystal fibers. TIR occurs when light propagating in an optically dense medium hits a boundary of a less dense medium, at an angle smaller than what is called the critical angle. The critical angle can be found through Snell's law of refraction

$$n_1 \sin\theta_1 = n_2 \sin\theta_2, \tag{2.1}$$

where $n_{1,2}$ are the refractive indices of the two mediums, and $\theta_{1,2}$ are the incident and transmitted angle, respectively. The critical angle can be found by setting the transmitted angle to 90°, $\theta_2 = 90°$, and solving for the incident angle, θ_1. The result is

$$\theta_c = \arcsin\left(\frac{n_2}{n_1}\right), \tag{2.2}$$

and as long as the incident angle is smaller than the critical angle, $\theta_i < \theta_c$, TIR will occur.

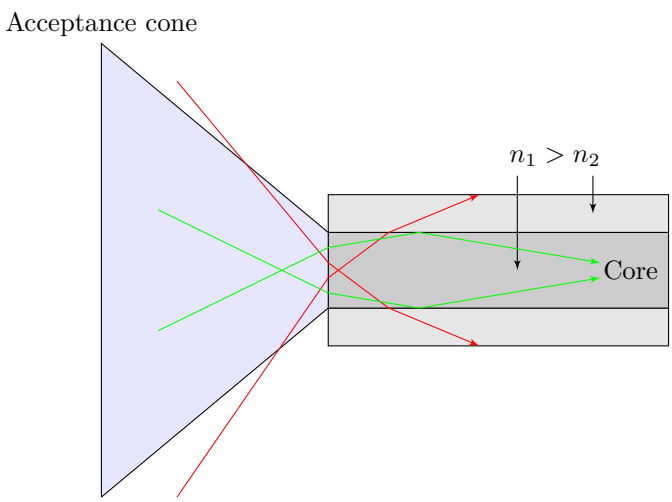

Figure 2.1: Side view of an optical fiber, illustrating the acceptance cone and how the light propagates in the different layers.

Since two mediums are needed in order to achieve TIR, the typical optical fiber contains two layers. The two layers are called core and cladding, and are illustrated in figure 2.1. The refractive index of the core has to be greater than the refractive index of the cladding in order to confine the light in the core. This difference in refractive index is what defines the guiding properties and is usually expressed as the numerical aperture (NA), which is defined as the sine of half of the acceptance angle of the fiber;

$$\mathrm{NA} = \sin\theta_{\mathrm{a}}. \tag{2.3}$$

An analytical expression for the NA can be derived from Snell's law (2.1). Let θ_{a} be the maximum angle which allows TIR and θ_{r} be the reflected angle;

$$n_0 \sin\theta_{\mathrm{a}} = n_1 \sin\theta_{\mathrm{r}}, \tag{2.4}$$

and through geometry, see figure 2.2, can $\sin\theta_r$ be expressed as $\sin(90^\circ - \theta_{\mathrm{c}}) = \cos\theta_{\mathrm{c}}$ where θ_{c} is defined in (2.2). Therefore can (2.4) be written as

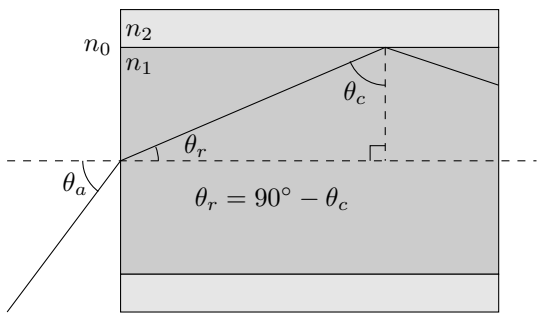

Figure 2.2: Geometry of light in an optical fiber.

$$\frac{n_0}{n_1}\sin\theta_{\mathrm{a}} = \cos\theta_{\mathrm{c}}. \tag{2.5}$$

By squaring both sides and using the Pythagorean trigonometric identity

$$\frac{n_0^2}{n_1^2}\sin^2\theta_{\mathrm{a}} = 1 - \frac{n_2^2}{n_1^2} \tag{2.6}$$

is obtained. By solving (2.6) for $n\sin\theta_{\mathrm{a}}$ and assuming that the surrounding medium is air ($n_0 = 1$);

$$\sin\theta_{\mathrm{a}} = \sqrt{n_1^2 - n_2^2} = \mathrm{NA} \tag{2.7}$$

is obtained. This shows that a large NA implies that incoming light will be guided in the fiber despite very wide angles. The opposite of this, for a small NA, the incident light must be very close to normal incidence in order to be guided. One might think that the higher the NA the better, but a high NA causes higher scattering losses from greater concentrations of dopant [10], which increase the core index.

Essentially, fibers are cylindrical waveguides which allows the finding of analytical solutions to the Maxwell equations. These solutions, or modes, are all discrete sets of electro-magnetic field distributions that propagate parallel to the fiber axis and are therefore guided. It turns out that the NA, together with the core radius, r_c, actually determines the number of modes supported by the waveguide. The normalized frequency number, or V-number, is defined as

$$V_{\mathrm{nr}} = 2\pi \frac{r_c}{\lambda} \mathrm{NA}_{\mathrm{core}}, \tag{2.8}$$

where λ is the wavelength in the core. When V_{nr} is smaller than 2.405 SM operation is obtained. The solution to Maxwell's equation for propagation in a cylindrical waveguide is the first root of the Bessel function, J_0, and its numerical value is the limit for SM operation, 2.405 [11].

Although a small NA and hence SM operation might be desired, too small NA yields diluted guiding properties and thus becomes sensitive to waveguide perturbations, such as bending. This fact is actually employed to obtain SM operation of slightly multi-mode fibers. When the fiber is bent, the more weakly guided higher-order modes will experience higher bending losses and thus SM operation will be favored in a tightly coiled fiber [12]. This technique to reduce the symmetry of the waveguide, and initiate losses for higher-order modes is called higher-order mode filtering.

2.1.2 Gaussian Beams

Laser beams can have different kinds of intensity distributions, however the Gaussian distribution is the most common. The beam width of a Gaussian beam can be expressed, with respect to the radius, ω, as

$$\omega(z) = \omega_0 \sqrt{1 + \left(M^2 \frac{z}{z_{\mathrm{R}}} \right)^2}, \tag{2.9}$$

where ω_0 is the beam waist radius, z_R is the Rayleigh range, M^2 is the beam quality factor, along the propagation length z. The beam waist is where the radius is the smallest, and the Rayleigh range is defined as the distance where the beam radius has increased by a factor of $\sqrt{2}$, defined as

$$z_\mathrm{R} \equiv \frac{\pi w_0^2}{\lambda}. \tag{2.10}$$

The introduced parameters are illustrated in figure 2.3, which describes how a Gaussian beam propagates.

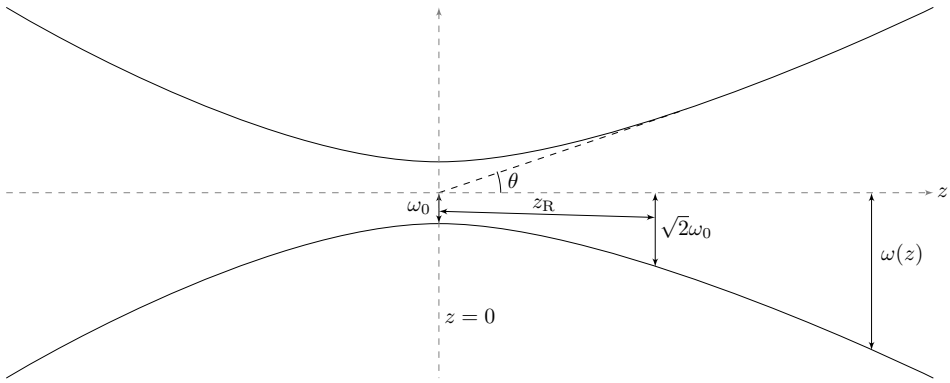

Figure 2.3: The beam propagation of a Gaussian beam.

It is well known that the local irradiance of a Gaussian beam at a given point can be expressed as

$$E = E_0 \exp\left(-\frac{4\rho^2}{D_\mathrm{L}^2}\right), \tag{2.11}$$

where ρ is the radial position of the point of interest to the center of the beam, and D_L is the beam diameter at $\frac{1}{e}$ of maximum irradiance, E_0. The total power in the beam, Φ_0, can be calculated with a double integral using polar coordinates;

$$\Phi_0 = \int_0^{2\pi}\int_0^{\infty} E_0 \exp\left(-\frac{4\rho^2}{D_\mathrm{L}^2}\right)\rho \,\mathrm{d}\rho \,\mathrm{d}\theta, \tag{2.12}$$

with the following substitution;

$$x = -\frac{4\rho^2}{D_\mathrm{L}^2} \Rightarrow \mathrm{d}x = -\frac{8\rho}{D_\mathrm{L}^2}\mathrm{d}\rho, \tag{2.13}$$

which yields

$$\Phi_0 = \frac{\pi E_0 D_\mathrm{L}^2}{4}. \tag{2.14}$$

Solving for E_0 gives an expression for the irradiance of the center of the beam,

$$E_0 = \frac{4\Phi_0}{\pi D_{\mathrm{L}}^2}. \tag{2.15}$$

2.1.3 Non-linear propagation effects

The technology of fiber optics has shown a promising development for quite some time. Earlier fiber attenuation and, sometimes, fiber dispersion were the limiting factors regarding the amount of data which could be transmitted in a single optical fiber. Today, the limiting factors are non-linear effects, such as some scattering processes and the fact that the refractive index of glass is dependent on the optical intensity going through the material. The latter phenomenon is called the Kerr effect, and is induced from a non-linear polarization that is generated in the medium. This causes a modification of the propagation properties of the light. It is minimized mainly by maximizing the effective area of the fiber, which is obvious when analyzing the general expression for the refractive index of the core in an optical fiber. The equation is

$$n = n_0 + n_2 \frac{P}{A_{\mathrm{eff}}}, \tag{2.16}$$

where n_0 is the refractive index of the fiber core at low optical power levels, n_2 the non-linear refractive index coefficient[1], P the optical power and $A_{\mathbf{eff}}$ the effective area of the fiber core. Another approach would be to minimize the optical power, this is however not always desirable.

The change in refractive index is however relatively small and induces non-linearities such as SPM and cross-phase modulation (XPM). The non-linearities which arise from scattering are of more interest. There are two types of non-linear scattering which are dominant in fibers, SRS and SBS.

Stimulated Raman Scattering

SRS is a non-linear scattering process involving optical phonons. One noticeable effect of this scattering is that longer wavelengths experience optical amplification at the expense of shorter wavelengths. This is due to the vibration of the glass lattice, and the lattice vibrations are excited which induces a rise in temperature.

[1] $2.35 \cdot 10^{-20}$ m^2/W for Si

The main process within Raman scattering is that a pump photon is converted into a low-energy photon signal, and the photon energy difference is carried away with a phonon. However, SRS is a weak effect in the CW regime, and the CW regime is capable of reaching very high-power.

Stimulated Brillouin Scattering

SBS is a non-linear scattering process involving acoustic phonons, in contrast to SRS where optical phonons are involved. The threshold of SBS is almost a thousand times lower than for SRS, and sets the upper limit of the optical power which can be effectively launched into a fiber, although there are situations where the SRS threshold is lower then the SBS threshold, i.e. for a broadband signal. If the optical power is above this threshold a part of the incident signal is scattered into the backwards direction after interacting with the phonons. The signal frequency will be downshifted. The counter-propagating wave can originally be very weak, but SBS has a strong non-linear optical gain for the back-reflected wave, and hence the wave can be amplified at suitable optical frequencies. The waves will generate a travelling refractive index grating, and this index grating will actually enhance the backwards reflection.

The beam which is reflected back will have a slightly lower frequency compared to the incident beam. This lower frequency is called Brillouin frequency, i.e. the frequency shift of the backwards signal with respect to the original signal, and is defined as

$$\upsilon_{\mathrm{B}} \equiv \frac{2n_{\mathrm{eff}}\upsilon_{\mathrm{A}}}{\lambda}, \tag{2.17}$$

where υ_{A} is the acoustic velocity. υ_{B} also depends on the material composition and to some extent the temperature and pressure of the medium.

There are several ways to increase the Brillouin threshold [3], i.e. to have a short fiber with a large mode area. Non-linear effects are intensity dependent, and by increasing the mode area, thus decreasing the intensity, the threshold of non-linear effects is increased. Longitudinal temperature variations, due to the fact that the speed of sound is temperature dependent, help to broaden and thus suppress SBS. Yet another technique is to manipulate the propagation of the acoustic wave by making the fiber core an acoustic antiguide in order to reduce the acousto-optic interaction.

2.2 Pumping scheme

In order to physically launch pump power into an optical fiber from free-space, certain conditions have to be fulfilled. Figure 2.4 is an illustration of relevant angles for focusing a beam in a fiber. The beam must be within the acceptance cone, which

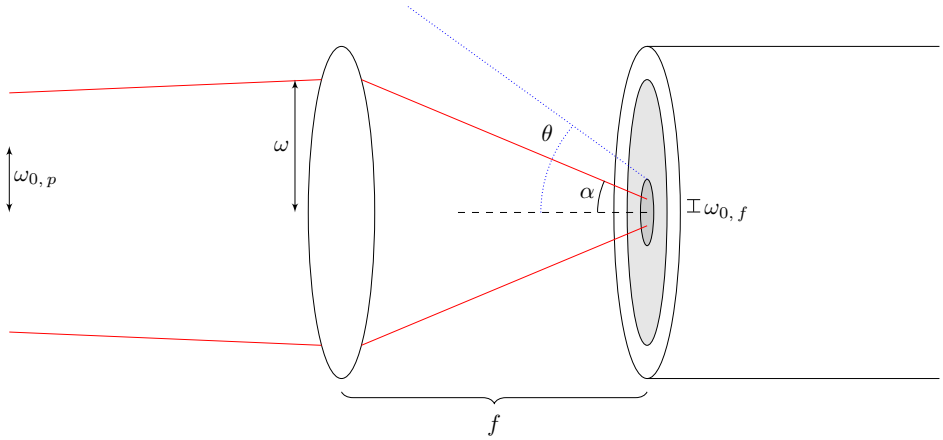

Figure 2.4: The geometry of focusing the pump into the core.

gives the condition $\alpha \leq \theta$. The geometry of figure 2.4 gives $\alpha = \arctan\left(\frac{\omega}{f}\right)$, and θ can be expressed with the NA, according to (2.3), as $\theta = \arcsin\left(\text{NA}\right)$. Solving for f yields

$$f \geq \frac{\omega}{\tan\left[\arcsin\left(\text{NA}\right)\right]}. \tag{2.18}$$

The other requirement in order to be able to focus the pump light into the fiber is that the spot size must be within the size of the core (or the inner cladding, depending on pump scheme). Therefore the beam area has to be smaller than core area (or inner cladding area). This gives $\pi\omega_{0,\,\text{f}}^2 \leq \frac{\pi d^2}{4}$, where $\omega_{0,\,\text{f}}$ is the beam waist at the focus and d is the core (or inner cladding) diameter. The beam waist at the focus, $\omega_{0,\,f}$, can be expressed as $\omega_{0,\,\text{f}} = \frac{\lambda f}{\pi\omega_{0,\,\text{p}}}$. Solving the inequality for f gives

$$f \leq \frac{\pi d\omega_{0,\,\text{p}}}{2\lambda}. \tag{2.19}$$

Therefore must the focal length of the lens be in the interval

$$\frac{\omega}{\tan\left[\arcsin\left(\text{NA}\right)\right]} \leq f \leq \frac{\pi d\omega_{0,\,\text{p}}}{2\lambda}. \tag{2.20}$$

There are several different pumping techniques and sources. In the early days of fiber lasers a flash lamp was used to pump the fiber transversely [13]. The technique which is by far the most common today is end-pumping with lasers. End-pumping, which was made possible by the introduction of the double-clad (DC) structure of optical fibers, is when the pump light is injected into the gain medium along the beam axis, i.e. longitudinal pumping. The DC fiber consists of a core, one inner, and one outer cladding. When the DC fiber is pumped, the pump light is launched into the inner cladding, closest to the core. The outer cladding is designed to obtain as much light as possible, and therefore has a high NA. One problem end-pumping might induce, is the separation of the pump light and the output signal. The output signal generally has a higher beam quality, and can thereby destroy the pump source if it is allowed to be coupled back into the pump. Most often a dichroic mirror is used to separate the two signals.

There are several different kinds of end-pumping, e.g. cladding- and core-pumping. Cladding-pumped fibers have its pump light injected in its cladding, and core-pumped in the core. Laser diodes, which are low brightness sources, can be launched into the fiber with high efficiency given that the claddings have a high NA. Cladding-pumping became available when the first DC-fibers were introduced. A multimode pump source can produce an SM output, because the pump light, which is launched into the inner-cladding, is confined by the outer-cladding. As the pump light propagates in the fiber, the doped core absorbs the light [3]. The opportunities to power-scale lasers are almost exclusively available for cladding-pumped systems [14]. According to Zhao *et al*, the core will help to promote efficient pump absorption in a cladding pumped fiber configuration, and therefore are higher slope efficiencies obtained with a cladding-pumped system [15].

Another sort of pumping is the so called in-band pumping. In-band pumping is when ions are directly pumped from the ground-state to the upper laser-level. One technique which uses this is tandem-pumping. Tandem-pumping is when the pump wavelength is close to the emission wavelength and the source has high brightness. When the pump light is close to the emission wavelength the quantum defect heating is low, thus suppressing the thermal load, and a high slope efficiency is obtained [3]. This can however induce some problems mentioned earlier regarding destroying the pump source due to the fact that the output signal is coupled back to the source. Since the pump wavelength and the output wavelength basically are the same, a

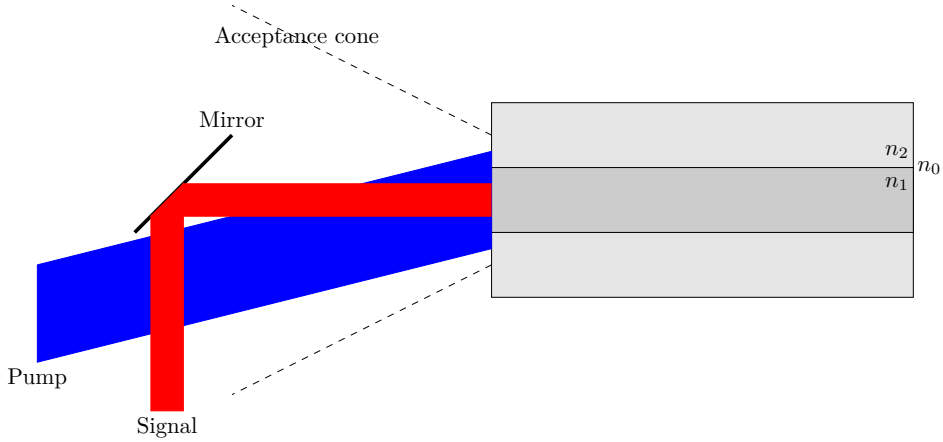

Figure 2.5: Skew-angle pumping.

dichroic mirror might not do the job. There are however good dichroic mirrors for this purpose, and a technique called skew-angle pumping can be implemented in the case of lack of high performance dichroic mirrors. The output and the pump are separated spatially, according to figure 2.5. One criteria which has to be fulfilled in order to skew pump an optical fiber is that the convergence angle must be smaller than the difference between the acceptance angle of the cladding and the acceptance angle of the cone. The acceptance angle is θ_{a}, defined from the NA, $\theta_{\mathrm{a}} = \arcsin(\mathrm{NA})$, see (2.3).

Chapter 3

Narrowband Thulium Fiber Lasers

3.1 Thulium

Tm is a RE element with atomic number 69. Tm can be pumped at several different wavelength bands, which are located at 793 nm, 1210 nm and at 1640 nm. Tm-doped Si-fibers have a very broad emission spectrum for the ${}^3F_4 \rightarrow {}^3H_6$ transition. The

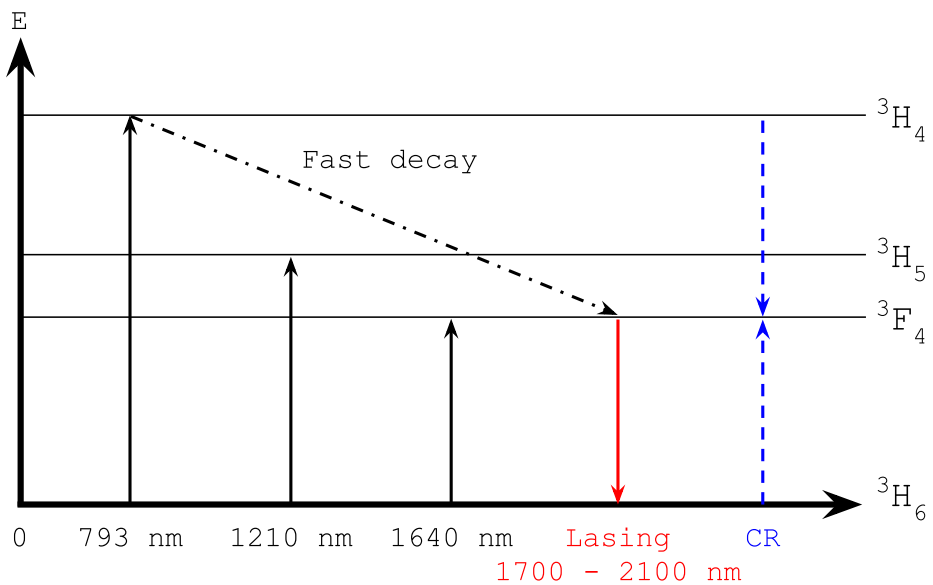

Figure 3.1: Energy level diagram of thulium in a silica fiber.

span is about 400 nm, ranging from 1700 nm to 2100 nm which provides a wide flexibility in operating wavelength. This is due to the Tm ions interaction with the local crystal field, its energy levels Stark split into broad energy bands, which is an inhomogeneous broadening effect [16]. The increased phonon energies due to temperature changes also contribute to this broadening [17]. The energy spectra of Tm in Si can be seen in figure 3.1, with the sub-levels of the different energy levels left out, because line broadening mechanisms create manifolds [13]. The lasing transition from ${}^3F_4$ to ${}^3H_6$, is broad due to these sub-levels, and the sub-levels are susceptible to temperature changes, just as the phonon energy, which induce a redistribution of the populations. The ions relax down from the bottom of ${}^3F_4$, to the different sub-levels of ${}^3H_6$, thus enabling the broad emission spectrum. Since ${}^3H_6$ is the ground state, the transition of Tm-doped fiber lasers is considered to be a quasi-three level transition. However, at laser transitions beyond 2020-2030 nm, the sub-levels of the top of ${}^3H_6$ are not highly thermally populated, thus acting as a quasi-four level transition [13].

According to figure 3.2, there is an absorption peak around 1600 nm. If the

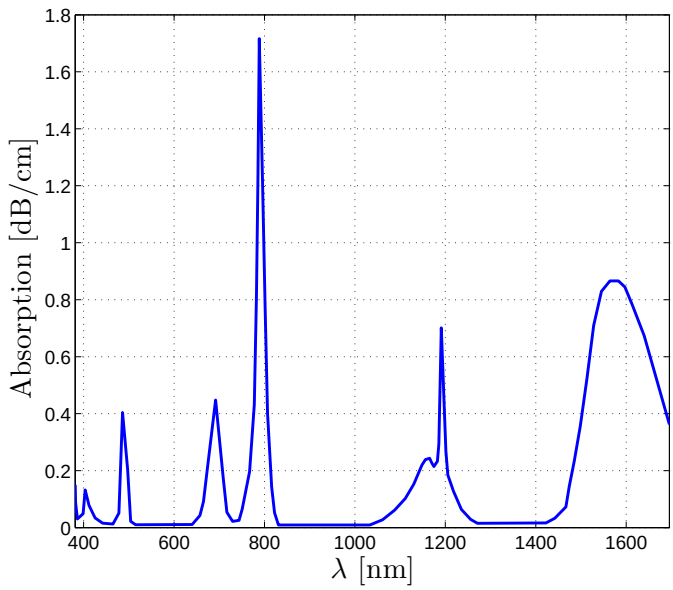

Figure 3.2: Absorption spectra of thulium in silica fibers.

system is pumped with, for instance an Er-laser, the ion is excited directly to the

laser level $^3F_4$, and thus is an in-band pumping scheme. Pumping at 793 nm is better however, since there are cheap high-power diode lasers commercially available in the near-infrared (NIR) region. In addition to this, Tm has a strong absorption peak at 793 nm, and a phenomenon called cross-relaxation (CR) can be exploited to improve the quantum efficiency. Geng *et al* showed in 2007 that a theoretical quantum efficiency of 200% can be obtained for 2 μm laser operation [18]. The absorption and emission cross section at the upper laser level ($^3F_4$), is plotted in figure 3.3. Since there is a spectral overlap between the two, there is a chance of

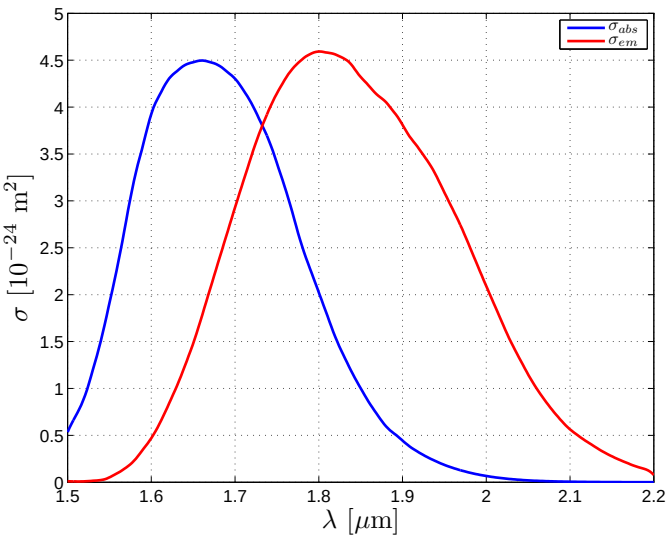

Figure 3.3: Absorption and emission cross-section of the upper laser level, $^3F_4$, of thulium in silica.

reabsorption.

CR is a dipole-dipole interaction between adjacent Tm ions, and occurs due to spectral overlap between the absorption transition, $^3H_6 \rightarrow^3 F_4$, and the $^3H_4 \rightarrow^3 F_4$ and $^3F_4 \rightarrow^3 H_6$ emissions. It is called 2-for-1 CR, due to the fact that two 2 μm photons can be produced at the expense of one pump photon. When Tm is pumped at 793 nm, an ion is excited to the $^3H_4$-level, and when the ion relaxes down from the pump level to the lasing level ($^3F_4$) through non-radiative relaxation, it shares energy with an adjacent ion in the ground state ($^3H_6$) through CR, which also is excited to the $^3F_4$-level.

A lower limit for the CR-efficiency, η_{CR}, can be estimated to the slope efficiency, η_{s}, as

$$\eta_{\mathrm{CR}} = \frac{\eta_{\mathrm{s}}}{2}\frac{\lambda_{\mathrm{s}}}{\lambda_{\mathrm{p}}}, \tag{3.1}$$

where $\lambda_{\mathrm{s,p}}$ is the signal and pump wavelength, respectively [19]. CR is a Förster energy transer, and depends strongly on the distance between the ions, and therefore also on the dopant concentration [13].

Moulten *et al* [20] noted that there is no real transition possible from the ${}^3H_4$-level to a higher Tm level when directly pumped at 790 nm and according to Jackson *et al* [21], the maximum theoretical slope efficiency is about 40%, in the absence of CR, and the minimum threshold pump power about $17 - 18$ mW at a pump wavelength between 785 and 795 nm.

3.2 Spectral control

As the lasing wavelength approaches 2 μm, the transparency of Si becomes increasingly poor due to infrared (IR) absorption (vibrational resonances dominate), see figure 3.4. At shorter wavelength Rayleigh scattering is the dominating loss, introduced

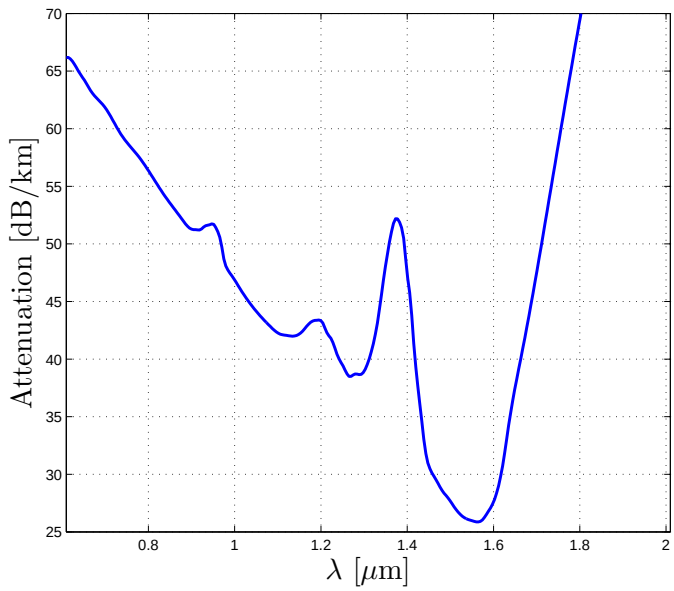

Figure 3.4: Attenuation in a silica fiber depending on wavelength.

by density fluctuations of the glass. Si has a minimum loss around 1.55 μm , and therefore communication fibers are designed for that wavelength.

An alternative to the Si-based fibers are the fluoride based fibers. Although a more efficient operation can be obtained, there are several downsides. Fabrication, aging of the host material, hygroscopicity and low pump power damage threshold are a few examples [22].

3.2.1 Fiber Bragg gratings

The FBG is an optical device which in principle acts as a mirror for desired wavelengths, and was chosen as the wavelength selecting element. The first FBG was demonstrated by Ken Hill in 1978, and was actually called Hill grating [23]. Hill *et al* noticed how the reflectivity intensity in a Germanium-doped fiber increased with time when irradiated with an intense Argon-ion laser, as they investigated non-linear processes in the mentioned fiber. The phenomena was explained as an unknown photosensitivity, and of course caught the interest of others. Eventually it was shown that the process was a two-photon mechanism, since the grating strength increased as the square of the light intensity [24].

The Hill grating arose through Fresnel reflection at the fiber end, which induced a standing wave pattern and index modulation was introduced. Hill *et al* used radiation at 488 nm, but Meltz *et al* showed in 1989 that irradiating the fiber with 244 nm was far more effective [25], due to Si's absorption peak. With this lower wavelength, a FBG could be manufactured with two intersecting beams at any desired wavelength. They also used a new technique called transverse holographic method, which irradiates the fiber from the side, rather than along the fiber axis.

Ultraviolet (UV) light is often used to fabricate FBGs, and there are two possibilities to use the radiation, either through a phasemask or by using two-beam interference [25]. In the case of the phasemask, the phasemask will create an interference pattern which determines the index modulation. The zeroth order of the diffracted beam is practically cancelled out, and it is often only the first, and in some cases the second, order which are maximized. The phase mask technique is considered to be one of the simplest and most stable methods of creating FBGs. Chirped gratings can be produced by altering the distance between the interference fringes, which is difficult to do with a phase mask. One of its biggest drawbacks is

the lack of tuneability in the inscribed Bragg wavelength, since it depends primarily on the periodicity of the phasemask [26].

The interference technique is used for other types of FBGs, and the index modulation is induced by the increased intensity at the interference point. The modulation of refractive index only occurs in the core of the optical fiber since the fiber cladding is transparent to the UV light whereas the fiber core is highly absorbing to the UV light [23]. At wavelengths shorter than 244 nm, there is no need for sensitization, if however sensitization is needed it is often done with hydrogen (H)-loading.

There are two different kinds of interferometric techniques; amplitude- and wavefront-splitting. This thesis will not go in depth within these fields, I will however mention that the Bragg wavelength can be altered by adjusting the incident angle of the UV beams.

Yet another technique, is the point-by-point (PbP) technique. Instead of UV light, IR light is used, which is sent in intense femtosecond pulses transversal to the fiber. When the IR light is focused, a two-photon absorption occurs, which is a mix of tunnel ionization, avalanche ionization, and multi-photon ionization, and thus changes the refractive index. Since the repetition rate of the pulses is well known, the velocity by which the fiber is translated defines the Bragg wavelength, and can therefore easily be altered without changing any of the components. This is one of the main advantages of the PbP-technique, but also that densification effects induce a high thermal tolerance. The lack of sensitization and its wide flexibility are also huge benefits. Since this technique is a step-by-step procedure the production time is rather high [26].

Theoretical approach

FBGs are optical elements in fiber optics which reflect certain wavelengths and transmit all others. During this thesis the FBG is used as cavity mirror and wavelength-locker, simultaneously. The fundamental mechanism behind the FBGs is Fresnel reflection. When light switches from one medium to another with a different refractive index, the light can both reflect and refract.

The FBG is periodic or aperiodic perturbation of the effective refractive index in the core of an optical fiber [27]. A schematic structure of a FBG can be seen in

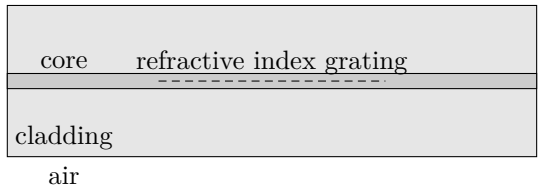

Figure 3.5: Schematic structure of a fiber Bragg grating.

figure 3.5 and figure 3.6 shows how the effective refractive index is modulated. If the Bragg condition is satisfied the refractive index perturbation leads to the reflection of light in a narrow range of wavelengths. The Bragg condition is defined as

$$\frac{2\pi}{\Lambda} = 2 \cdot \frac{2\pi n_{\text{eff}}}{\lambda} \Rightarrow \lambda = 2n_{\text{eff}}\Lambda, \tag{3.2}$$

where n_{eff} is the effective refractive index of the fiber, Λ the grating period and λ the vacuum wavelength.

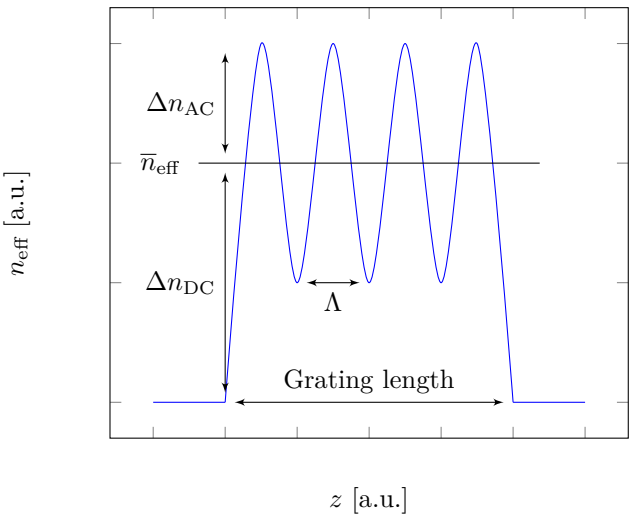

Figure 3.6: Shows the modulation of the effective refractive index along the z-axis.

To derive the Bragg condition, one may start with the grating equation

$$n \sin\theta_2 = n \sin\theta_1 + m\frac{\lambda}{\Lambda}, \tag{3.3}$$

which essentially describes how an incident light wave at an incident angle of θ_1 behaves. It is also capable of predicting the direction of the constructive interference,

and more importantly the wavelength at which the fiber grating most efficiently couples light between two modes. θ_1 is as mentioned the incident angle, θ_2 the angle where the constructive interference occurs and m is the diffraction order, see figure 3.7. By using the propagation constant β, the grating equation can be written as

$$\beta_2 = \beta_1 + m\frac{2\pi}{\Lambda}, \tag{3.4}$$

since $\beta = \frac{2\pi}{\lambda} n_{\text{eff}}$ and $n_{\text{eff}} = n_{\text{co}} \sin\theta$. Negative values of β correspond to light waves propagating in the $-z$-direction while positive β correspond to the z-direction. Since we are talking about short-period (reflection) gratings, $\beta_2 < 0$, (3.4) can be written as

$$-\beta_2 = \beta_1 - \frac{2\pi}{\Lambda}, \tag{3.5}$$

where $m = -1$ represents the first diffraction order which usually is dominant in a fiber. If $\beta = \frac{2\pi}{\lambda} n_{\text{eff}}$ is inserted in (3.5) and solved for λ one arrives at

$$\lambda = (n_{\text{eff},1} + n_{\text{eff},2})\Lambda, \tag{3.6}$$

which is the resonant wavelength for the reflection of a mode of index $n_{\text{eff},1}$ into a mode of index $n_{\text{eff},2}$. If however the two modes are identical, one arrives at the Bragg condition, which is also known as the Bragg reflection [28].

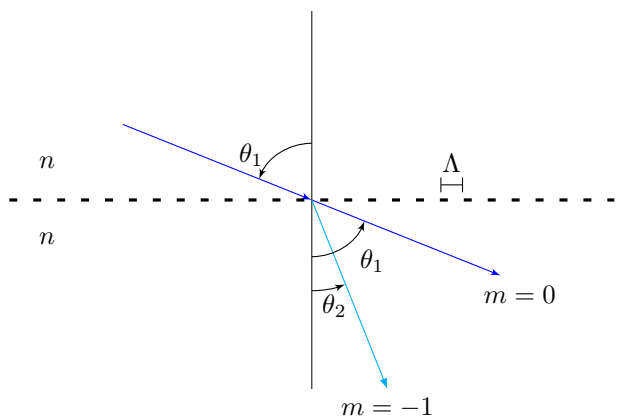

Figure 3.7: How a light wave is diffracted by a grating.

The physical interpretation of the Bragg condition is that the difference of the wave vectors for the reflected and incident waves must match the wavenumber of

the grating. If this condition is not fulfilled the light will travel through the FBG with minimal effort, and hence continue to propagate forward. There are however measurable effects in the form of side lobes in the reflection spectrum.

When a FBG is designed for a narrowband fiber laser it is important that the FBG has a narrow reflection bandwidth. This is obtained for long gratings with weak index modulation. The normalized bandwidth ($\Delta\lambda/\lambda$) can be as low as 0.1, or even 10^{-4}.

One common technique to increase the absorption of the FBG inscribing UV light, is to load the fiber with H in order to increase the photosensitivity [26]. The photosensitivity depends on the chemical composition, as well as the wavelength, and Si naturally has a low photosensitivity.

Diffraction efficiency and spectral dependency of FBGs can be derived using coupled-mode theory (CMT), which is the most common technique because of its accuracy and intuitiveness. The CMT assumes that the transverse component of the electric field can be written as a superposition of the ideal modes [28], and require that the energy and momentum is conserved [29] since the modes in an ideal waveguide are orthogonal. This method also assumes that the perturbation of the refractive index is expressed as

$$\delta n_{\text{eff}}(z) = \overline{\delta n}_{\text{eff}} \left(1 + v \cos \left[\frac{2\pi}{\Lambda} z + \varphi(z) \right] \right), \tag{3.7}$$

where $\overline{\delta n}_{\text{eff}}$ is the dc index change spatially averaged over a grating period (see figure 3.6), v is the fringe visibility of the index change and $\varphi(z)$ describes the grating chirp. The dominant interaction in a FBG is between a reflection of a certain mode with amplitude $A(z)$, with an identical counter-propagating mode of amplitude $B(z)$. Their relation can be simplified to only contain the amplitudes of the particular mode through CMT, and the synchronous approximation [30]. By neglecting the fast oscillating amplitude terms, the forward and backward propagation amplitudes A, and B, can be replaced by $R(z) \equiv A(z) \exp(\mathrm{i}\delta z - \varphi/2)$ and $S(z) \equiv B(z) \exp(-\mathrm{i}\delta z + \varphi/2)$, in order to incorporate the detuning delta from signal wavelength and Bragg wavelength. The two amplitudes then couple according to

$$\frac{dR}{dz} = \mathrm{i}\hat{\sigma} R(z) + \mathrm{i}\kappa S(z), \tag{3.8}$$

and

$$\frac{dS}{dz} = \mathrm{i}\hat{\sigma}S(z) + \mathrm{i}\kappa^* R(z), \tag{3.9}$$

where κ is the ac coupling coefficient, which is determined by the overlap integral of the core and cladding mode and by the amplitude of the periodic modulation of the mode propagation constants. $\hat{\sigma}$ is the general dc self-coupling coefficient defined as $\hat{\sigma} \equiv \delta + \sigma - \frac{1}{2}\frac{d\varphi}{dz}$, and δ is the detuning wave scalar, expressed as

$$\delta \equiv \beta - \frac{\pi}{\Lambda} = 2\pi n_{\mathrm{eff}} \left(\frac{1}{\lambda} - \frac{1}{\lambda_{\mathrm{D}}} \right), \tag{3.10}$$

The design wavelength, λ_{D}, is defined as

$$\lambda_{\mathrm{D}} \equiv 2n_{\mathrm{eff}}\Lambda, \tag{3.11}$$

and if $\delta = 0$ one finds the Bragg condition (3.2). σ is the dc coupling coefficient which is a complex number, and its imaginary part is the absorption coefficient in the grating. The non-reflected light will have a transmission loss dependent on the dc coupling coefficient. The last term of $\hat{\sigma}$ describes possible chirp of the grating period. Since this thesis treats uniform FBGs the perturbation of the refractive index is constant and $d\varphi/dz = 0$, which indicates that κ, σ and $\hat{\sigma}$ are constant along the grating [28]. σ and κ are found to be

$$\sigma = \frac{2\pi}{\lambda}\overline{\delta n}_{\mathrm{eff}}, \tag{3.12}$$

and

$$\kappa = \kappa^* = \frac{\pi}{\lambda} v \overline{\delta n}_{\mathrm{eff}}. \tag{3.13}$$

Now (3.8) and (3.9) are coupled first-order ordinary differential equations with constant coefficients, which can be solved given that appropriate boundary conditions are specified. Analysis shows that the maximum reflectivity is [23, 26, 28]

$$r_{\max} = \tanh^2(\kappa L), \tag{3.14}$$

where L is the length of the fiber and κ as mentioned earlier is the ac coupling coefficient between the forward and the backward propagating modes. The maximum reflectivity $r_{\max}$ occurs at a certain wavelength, which can be determined through the following equation;

$$\lambda_{\max} = \left(1 + \frac{\overline{\delta n}_{\mathrm{eff}}}{n_{\mathrm{eff}}} \right) \lambda_{\mathrm{D}}, \tag{3.15}$$

as long as $\hat{\sigma} = 0$. If N is the total number of grating periods, the reflection bandwidth is smaller for greater N, and vice versa.

There are several different techniques to fabricate FBGs. One common technique is to use UV light and expose the fiber core with two beams. The interferometric superposition of the UV beams will be absorbed and free electrons will actually cause some composition change, which leads to a permanent index change. One can also use one beam, and a phase mask to create two beams. In that case usually only the two first order-diffracted beams are used. An alternative to UV light is IR light. When exposing the core with IR light, once again a phase mask can be used, or femtosecond pulses can be used in the PbP-technique.

When fabricating FBGs with the PbP-technique, it is important that only the core is in the focus of the pulses, which requires high precision alignment. If the cladding is within the pulses focus, the cladding is subjected to the refractive change as well. According to Kondo *et al* [31] formation of localised plasma in the bulk of the material causes densification of the bulk and therefore induces a refractive index change. Since this process involves a highly non-linear photo-ionisation a dense focused laser beam has to be achieved since this entails a high intensity. This phenomena is reported in several other articles, for instance [32].

The densification occurs due to thermal effect when exposing the core with femtosecond pulses, and therefore the FBG has increased thermal properties compared with FBGs manufactured with UV-radiation. When the core is exposed to UV light, the densification arises from structural changes due to electron transfer from Ge-related defects rather than thermal defects.

Kondo *et al* [31] found that the temperature dependence of the wavelength to be

$$\frac{\mathrm{d}\lambda_\mathrm{p}}{\mathrm{d}T} = \frac{\Lambda_\mathrm{p}}{\mathrm{d}T}\Delta n + \Lambda\frac{\mathrm{d}\Delta n}{\mathrm{d}T}, \tag{3.16}$$

where λ_p is the peak wavelength.

One of the main advantages of the PbP-technique is that it is fairly easy to adjust the grating period Λ, and therefore also the resonance wavelength (see (3.2)). Adjustment of the grating period is discussed further in appendix D. The non-linear absorption of the femtosecond pulses is another advantage. Since it is a multi-photon process it requires high power densities and can thus surpass material-dependent thresholds. If the absorption would have been linear, inscribing

fine periodic structures would not have been achievable. The PbP-technique can be used in active fibers, as photosensitizing, for instance by hydrogenation, is not needed. The typical inscription time is also reduced from tens of minutes to tens of seconds.

There are however disadvantages, most of them involving focusing and aligning the beam. As mentioned earlier the beam has to be focused into the core, and the optical alignment has to be maintained as the focus position is moved along the fiber. This requires high-quality translation stages. There are also restrictions regarding the laser pulse power. The power density in the focal point has to be high enough to change the refractive index, and meanwhile low enough to avoid material damage [31].

3.3 Modelling

A numerical model of a physical system is of great use in order to develop and understand the given system. To develop a proper numerical model of any laser the systems rate equations are needed. The rate equations describe how the populations in the different energy levels vary over time, and what effects may influence these populations. Often it is sufficient to use a two level model to simulate the system, and the populations of interest are thereby N_1 and N_2 (where $E_2 > E_1$), provided that the decay from level three, the $^3H_4$-level in the case of Tm pumped with 793 nm, is fast.

The Giles parameters are often used for modeling fiber lasers with RE elements as dopant. According to Giles *et al.* [33], the amplified power for a signal can be written as

$$P(L) = P(0) \exp\left[\int_0^L \{g^*(\lambda)N_2(z) - \alpha(\lambda)N_1(z)\}\, dz\right], \tag{3.17}$$

where $P(0)$ is the initial power, L is the fiber length, N_1 and N_2 are the lower and upper laser levels respectively, and $g^*(\lambda)$ and $\alpha(\lambda)$ are the Giles parameters, which describe the gain and absorption, and are defined as

$$g^*(\lambda) = \Gamma(\lambda)\sigma_{21}(\lambda)N_{\text{tot}}, \tag{3.18}$$

and

$$\alpha(\lambda) = \Gamma(\lambda)\sigma_{12}(\lambda)N_{\text{tot}}. \tag{3.19}$$

The overlap coefficient, Γ, which describes the overlap between the normalized optical mode and the dopant distribution in the fiber is often set to one. This corresponds to a perfect overlap of the optical mode with the doped region. The emission and absorption cross-section are σ_{21} and σ_{12} respectively, and N_{tot} the density of the dopant in the core.

The numerical model used to simulate the TFL cavity is a slightly modified version of a Yb-model developed by Zeil [34]. The model solves the boundary value problem of a linear cavity laser by substituting the problem with two initial value problems, by applying the two following conditions;

- the forward signals $(z = L) = R_L \times$ the backward signals
- backward signals $(z = 0) = R_0 \times$ the forward signals

where R_0 and R_L corresponds to the wavelength dependent reflectivities at position $z = 0$ and $z = L$ respectively, see figure 3.8.

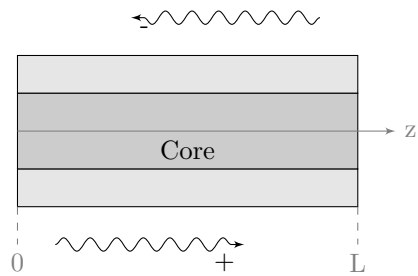

Figure 3.8: The sign convention of a beam propagating a length of L.

The rate equations which regulate the evolution of the pump and signal powers along the fiber can be expressed by dividing the amplified spontaneous emission (ASE) spectrum into N slots with bandwidth $\Delta\lambda$;

$$\frac{dP_i^{\pm}}{dz} = \pm\Gamma_i(\sigma_{21\ i}N_2 - \sigma_{12\ i}N_1)P_i^{\pm} \pm 2\sigma_{21\ i}\frac{N_2}{A_i}\frac{hc^2}{\lambda_i^3}\Delta\lambda \mp \alpha_i P_i^{\pm}, \tag{3.20}$$

and

$$N_2 = N_{\text{tot}}\left(\sum_i^N \frac{\Gamma_i\lambda_i}{hcA}\sigma_{12\ i}(P_i^+ + P_i^-)\right)\cdot\left(\sum_i^N \frac{\Gamma_i\lambda_i}{hcA}(\sigma_{12\ i} + \sigma_{21\ i})(P_i^+ + P_i^-) + \tau_{21}^{-1}\right)^{-1}, \tag{3.21}$$

where P_i is the power at wavelength λ_i, the total Tm-ion concentration expressed as $N_{\text{tot}} = N_1 + N_2$. A_i is the transversal mode area, which can be approximated with the core area and cladding area for signal and pump radiation, respectively. A is the doped area of the fiber and τ_{21} the excited-state lifetime. The term α_i accounts for losses and the signs $\pm$ refer to either forward or backward propagation of the beams, according to figure 3.8. The boundary conditions are

$$P_i^+(0) = R_{1,i}\eta_{1,i}P_i^-(0), \tag{3.22}$$

$$P_i^-(L) = R_{2,i}\eta_{2,i}P_i^+(L), \tag{3.23}$$

and

$$P_{\lambda_p}^+(0) = P_p + R_{1,i}\eta_{1,i}P_i^-(0), \tag{3.24}$$

where R is the reflectivity of the wavelength selecting element, η coupling losses, λ_{p} pump wavelength, and P_{p} launched pump power. This is a boundary value problem, which is reduced to an initial value problem using a shooting method, and is thereafter solved with the numerical Runge-Kutta method of the fourth order, as suggested by [22] and [21].

Chapter 4

Experimental Setup

There are three essential parts which a laser consists of, which are the pump source, gain material and the cavity. In this chapter the pump source, including characterization, and the all-fiber cavity, including gain material, cavity delimiters, and wavelength selecting element will be discussed.

In the end of this chapter, the setup to remove residual pump is explained, which lets the user investigate the output signal.

4.1 All-fiber laser cavity

The all-fiber cavity was pumped with a multimode laser diode (LD), with a pump power up to 3.3 W at 793 ± 0.1 nm. The passive delivery fiber of the LD was spliced to a highly reflective (HR) FBG, which acted both as input coupler and wavelength selecting element. The FBG was in turn spliced to the active Tm-fiber

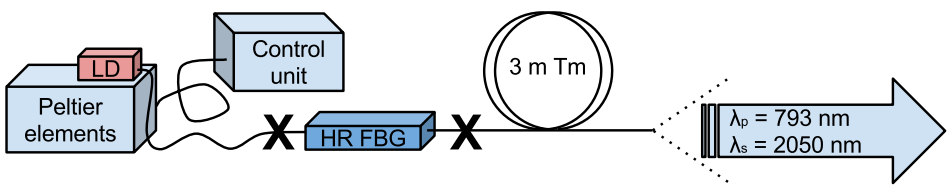

Figure 4.1: The setup of the thulium fiber laser, where the X's indicate the splices.

which was used as gain material. As output coupler the Fresnel reflection of the

perpendicularly cleaved gain fiber end was used. The complete setup can be studied in 4.1.

4.1.1 Pump source

The TFL was pumped with a multimode LD module (BMU3-793-02-R from Oclaro) with an optical wavelength of $790.4 \pm 2.3\,\text{nm}$. It is designed with an E2 front mirror passivation that prevents catastrophic optical damage, and provides high output powers (up to 3.5 W) which are stable with both time and temperature. Since the conversion of electrical to optical energy in the LD induces heat generation, which alters the output characteristics, it was mounted on a heat sink for cooling purposes. The increased temperature will increase the bandgap in the semiconductor LD, and therefore the central wavelength will change with temperature and thus is heating control required.

The heat sink consisted of a heat reservoir in form of a 1 cm thick copper plate, where the LD was mounted. Three 3-by-3 cm Peltier elements were installed to electronically control the reservoir temperature through a control unit. The temperature was measured through a $10\,\text{k}\Omega$ (at $25\,^\circ\text{C}$) NTC thermistor placed on the surface of the copper plate. The pump light was delivered through a passive fiber with a core and cladding diameter of $105 \pm 3\,\mu\text{m}$ and $125 \pm 3\,\mu\text{m}$, respectively, and a core NA of 0.22.

Pump source characterization

As previously mentioned the conversion of electrical to optical energy in the LD will induce heat generation which alters the output wavelength. The output wavelength of the LD as a function of diode current, I_{LD}, with the NTC thermistor, R_{NTC}, kept constant is plotted in figure 4.2.

As I_{LD} increased, the output wavelength increased, while the full width at half maximum (FWHM) decreased, according to figure 4.3. The wavelength at $I_{\text{LD}} = 750$ mA was 789.1 nm (with a FWHM of 5.9 nm) and shifted 2.6 nm, to 791.7 nm (FWHM = 2.4 nm), at a pump current 4000 mA. This is due to the fact that the number of spectral lines that a laser is capable of supporting is a function of the operating current.

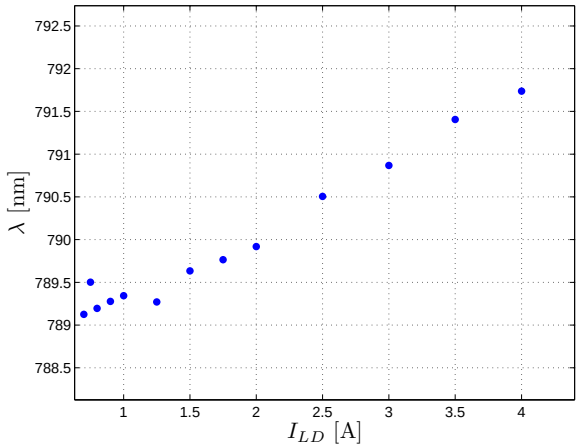

Figure 4.2: The wavelength peak variation of the pump diode with increasing diode currents, at a constant R_{NTC}.

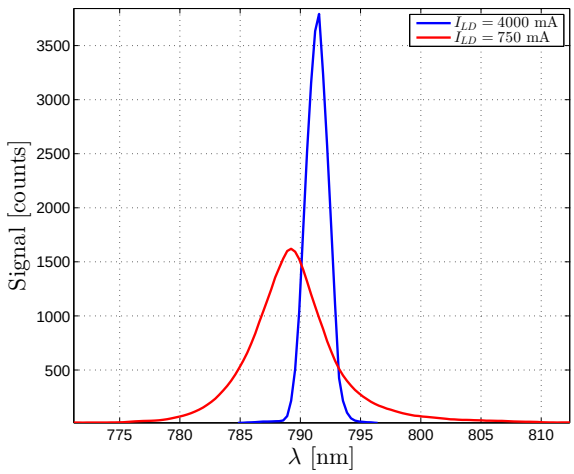

Figure 4.3: The wavelength peak variation of the pump diode with increasing diode currents, at a constant R_{NTC}.

The desired pump wavelength was 793 nm, and by altering the LD temperature (R_{NTC}) for each diode pump current, the output wavelength was fixed to 793 ± 0.1 nm. Figure 4.4 shows how R_{NTC} should be calibrated for each I_{LD} in order to obtain an output wavelength of 793 ± 0.1 nm.

The output of the multimode LD module, with the temperature calibrated for

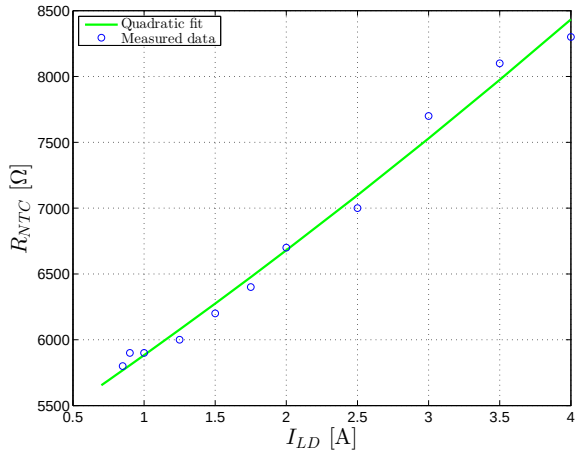

Figure 4.4: The NTC thermistor resistance versus the diode pump current to obtain an output wavelength of 793.0 ± 0.1 nm.

each I_{LD} to obtain the desired pump wavelength, is plotted in figure 4.5. The

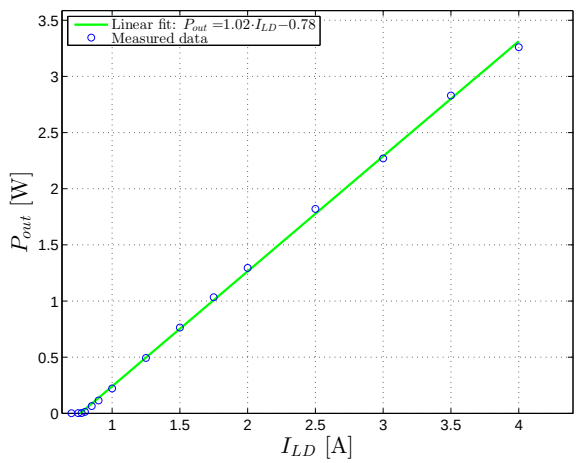

Figure 4.5: Output power from the laser diode versus the pump current at 793.0 ± 0.1 nm.

maximum pump power was 3.26 W, with a threshold current, I_{th}, of 765 mA.

4.1.2 Gain fiber

The gain fiber was 3 m of active Tm-fiber (SM-TDF-10P 130-HE from Nufern), with a core and cladding diameter of $10 \pm 1\,\mu$m and $130 \pm 2\,\mu$m, respectively, and a core NA of 0.15. The fiber had a cladding absorption of 3 dB/m at 793 nm, and was non-polarization maintaining (non-PM). The dopant concentration of Tm was about 1 mol%. The coiling diameter of the gain fiber, ϕ, was used as a variable and its effect on the TFL, in terms of change in pump absorption and modal quality of the laser signal, was also investigated.

4.1.3 Cavity delimiters

The delivery fiber of the LD was fusion spliced to the first cavity delimiter of the TFL, which was a 99.9% reflectivity FBG at 2050 nm with a reflection bandwidth of 1.5 nm (PWS-HPR 2050-1.5-99-10 / 125-0-1 from TeraXion). The fiber which the FBG was inscribed in had a core and cladding diameter of 10 μm, and 125 μm, respectively, with a core and cladding NA of 0.15 and 0.46. The second cavity delimiter, which acted as output coupler, was the Fresnel reflection of the perpendicular cleaved gain fiber end ($\approx 3\%$ reflection). All the splices were performed with an arc-charged fusion splicer (FSU 975 PM-A from Ericsson). The arc-fusion splicer charges up two electrodes, and the induced heat splices the two fibers into one fiber, with algorithms to calculate losses introduced by the splicing.

Another FBG was purchased, with a reflectivity of 12% (PWS-HPR 2050-0.6-12-10 / 125-0-1 from TeraXion) at 2050 nm. It may be used as an alternative output coupler, in later experiments.

4.2 Cladding pumped setup

The central wavelength of the 99.9% reflectivity FBG was 2050 nm, with a 95% reflection bandwidth of 1.5 nm. The fiber which the FBG was written on was a passive DC-fiber, with matching cladding diameter of the passive fiber of the LD, according to table 4.1. The FBG-fiber also had matching parameters with the active Tm-fiber, i.e. the cladding diameter and NA of the core.

The active fiber was a step-index, non-PM, DC-fiber with a cladding absorption of 3 dB/m at 793 nm, and a dopant concentration of about 1 mol%. Clustering of

Table 4.1: Fiber specifications relevant to the thulium fiber laser.

Fiber	Core ϕ	Core NA	Cladding ϕ	Cladding NA	Host
LD fiber	$105 \pm 3\,\mu$m	0.22	$125 \pm 3\,\mu$m	–	Si
FBG fibers	$10\,\mu$m	0.15	$125\,\mu$m	0.46	Ge+Si
Tm fiber	$10 \pm 1\,\mu$m	0.15	$130 \pm 2\,\mu$m	-	Tm+Si

Tm ions may occur, but can be suppressed by introducing aluminium (Al) ions thus enhancing the solubility of the Tm ions [19]. Since the core of the LD-fiber was greater than the core of the FBG-fiber, by an order of magnitude of approximately one, the TFL was cladding-pumped.

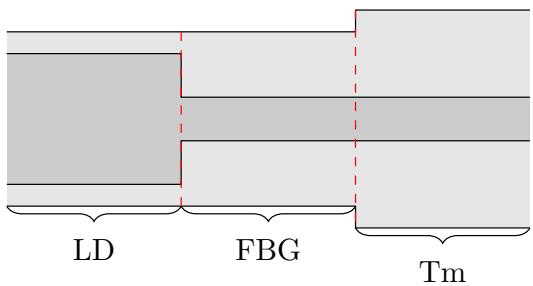

Figure 4.6: A not to scale schematic over the parameters of the three fibers used to develop the thulium fiber laser, indicating that the laser was cladding pumped. The red dashed lines indicates splicing.

Examining the different fiber parameters of table 4.1, it is intuitive why the TFL was cladding pumped. The incoming pump light travels through the fiber of the LD, with a big core, into the fiber of the FBG, with the same cladding diameter, but a much smaller core. The pump light eventually reaches the active fiber which has the same core diameter as the FBG-fiber, and a slightly wider cladding diameter. Figure 4.6 is a schematic over the different fiber parameters.

4.3 Laser characterization

Taking the diffraction of the laser signal into account, an appropriate collimating lens was chosen, with a focal length of 30 mm. After collimation, the signal was separated from the pump with two HR mirrors (from Layertec), according to figure 4.7. The residual pump was dumped, while the signal propagated to a detection

system of choice, D. During this thesis project several different detection systems were used, including a monochromator (iHR550 from Horiba), a power meter (XLPF12-3S-H2-DO from Gentec-EO), a Pyrocam (Pyrocam III from Ophiropt), and a spectrometer (AVS-USB2000 from Avantes).

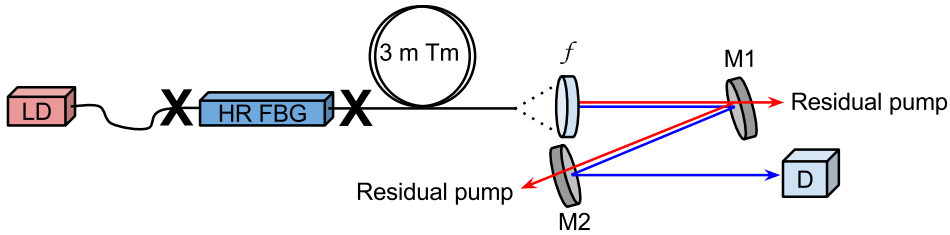

Figure 4.7: The setup used to characterize the thulium fiber laser. A lens with a focal length of 30 mm was used as collimator. Mirror M1 and M2 lets the signal hit a detection unit, D, while residual pump is removed.

Chapter 5

Experimental Results

In this chapter the experimental results will be presented. It includes power measurements, such as maximum output power, $P_{\max}$, threshold input power, P_{th} and slope efficiency, η_{s}. The laser polarization is also investigated, and also spectral and spatial characterization. In the section of spatial characterization there is a brief introduction to the beam quality factor, M^2, and also the knife edge technique, which is used to measure the beam radius and M^2.

5.1 Thulium fiber laser characterization

The maximum output power was 0.86 W, and the highest slope efficiency was 47%, both obtained with a coiling diameter of 3.5 cm. The slope efficiency gives a lower limit of the CR-efficiency, according to (3.1), of 61%. Since the active fiber was non-PM, the polarization was random, but the highest obtained polarization extinction ratio (PER) was 5.7 dB. Spectral characterization showed a central wavelength at 2051 nm, with a FWHM of 1.5 nm. The spatial characterization showed SM-operation with an $M^2 \leq 1.05$ in both the $x-$ and $y-$direction. Below follows a more in-depth description of the obtained results.

5.1.1 Power measurements

By investigating the output power of the TFL, at different input powers, several parameters could be determined, e.g. the slope efficiency, η_{s}, maximum output

power, $P_{\max}$, and the threshold input power, P_{th}. These parameters were measured both with respect to input power, and absorbed pump power, with the coiling diameter of the gain fiber, ϕ, as a variable. The output power with respect to input power is plotted in figure 5.1. The maximum output power of 0.86 W was obtained

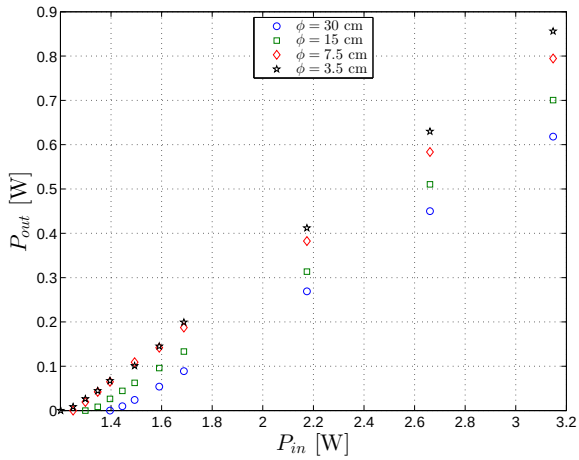

Figure 5.1: Output power with respect to input power.

with a coiling diameter of 3.5 cm. As ϕ increased, $P_{\max}$ decreased. The highest slope efficiency was 45%, also obtained with $\phi = 3.5$ cm. Since the lower limit of η_{CR} depends linearly on η_{s}, according to (3.1), the highest CR-efficiency was obtained with the same ϕ. As ϕ increased, η_{s} decreased.

The lowest threshold power was obtained with $\phi = 7.5$ cm, with a value of 1.24 W. These values are collected from figure 5.1 and tabulated in table 5.1.

Table 5.1: Thulium fiber laser characterization with respect to input power.

ϕ [cm]	3.5	7.5	15	30
η_{s}	45%	42%	38%	36%
P_{th} [W]	1.25	1.24	1.33	1.43
$P_{\max}$ [W]	0.86	0.79	0.70	0.62

When the output power was plotted with respect to absorbed pump power, the maximum output power remained unchanged, i.e. 0.86 W when $\phi = 3.5$ cm, according to figure 5.2. The slope efficiency, η_{s}, still decreased with increasing ϕ, but with an overall gain of the peak value. The highest slope efficiency was 47%,

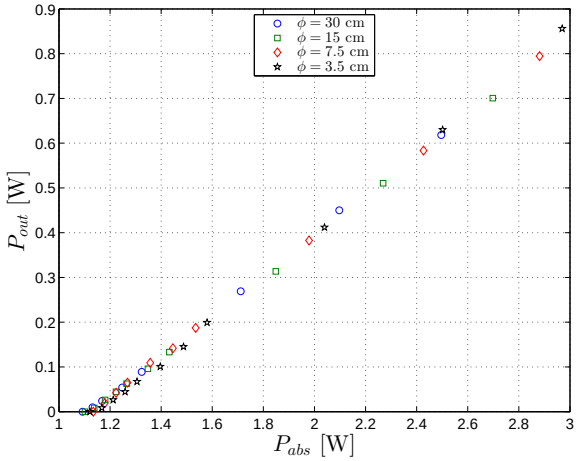

Figure 5.2: Output power with respect to absorbed pump power.

with $\phi = 3.5$ cm, just as in the previous case. The lowest threshold power was obtained with $\phi = 30$ cm, compared to 7.5 cm in the previous case. When the output power was plotted with respect to absorbed pump power, P_{th} strictly decreased with increasing ϕ. The parameters taken from figure 5.2 are tabulated in table 5.2. It is interesting to note that η_{s}, and P_{th} fluctuate less when plotted with respect to absorbed pump power, compared to with respect to input power.

Table 5.2: Thulium fiber laser characterization with respect to absorbed pump power.

ϕ [cm]	3.5	7.5	15	30
η_{s}	47%	45%	44%	45%
P_{th} [W]	1.17	1.13	1.13	1.12
P_{max} [W]	0.86	0.79	0.70	0.62

5.1.2 Laser polarization

Since the active fiber was non-PM, the polarization was random, and therefore also the PER. The maximum PER measured was 5.7 dB at ϕ= 15 cm and I_{LD}= 3500 mA. Depending on the fiber arrangements, different PERs were measured.

5.1.3 Spectral characterization

The optical spectrum was obtained by analyzing the output signal with a monochromator (iHR550 from Horiba), according to figure 4.7, where D is the monochromator. The scanning span was 1950-2200 nm, with a slit size of 1 mm, and integration time of 0.9 s. The resolution of the monochromator is the product of the slit size and 5.5 nm/mm, which yields a resolution of 5.5 nm. The spectrum is plotted in figure 5.3, and shows a central wavelength of 2050.8 nm. In the beginning of this section, the

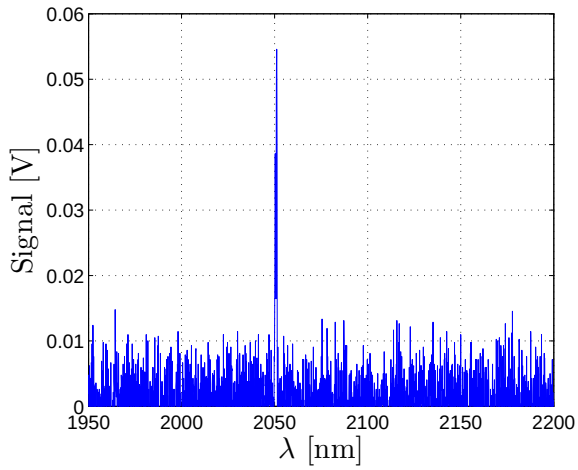

Figure 5.3: The spectrum of the output signal, with a peak at 2050.8 nm, FWHM of 1.5 nm, measured with a resolution of 5.5 nm.

FWHM is claimed to be 1.5 nm, which is less than the resolution. The reasoning for this claim is that 1.5 nm is the reflection bandwidth of the commercially obtained FBG.

5.1.4 Spatial characterization

This subsection will first introduce the concept of the beam quality factor, M^2, and also briefly explain the knife edge technique. Thereafter are the results of the spatial characterization presented.

Beam quality factor, M^2

The beam quality factor, or M^2-factor, describes the beam quality of a Gaussian beam. A perfect diffraction-limited Gaussian beam has a beam quality factor of $M^2 = 1$. This is derived from the fact that the M^2-factor is defined as the ratio between the product of the minimum value of the beam variance and the variance of the spatial frequency of the beam, and the corresponding product for a Gaussian beam [17];

$$M^2 = \frac{\sigma_{x0}\sigma_{s_x}}{[\sigma_{x0}\sigma_{s_x}]_G}. \tag{5.1}$$

Although the M^2-factor is a way to quantify the beam quality with a number, it is not sufficient to evaluate a beam's quality purely based on M^2.

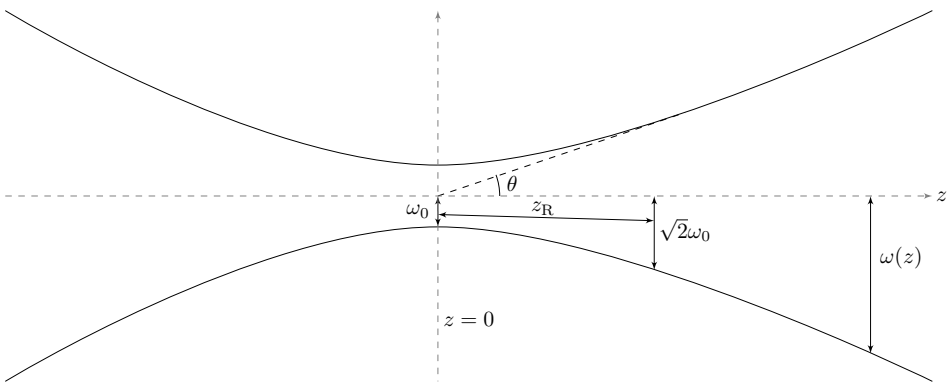

Figure 5.4: The beam propagation of a Gaussian beam (same as figure 2.3).

The different parameters can be seen in figure 5.4, and with the far-field approximation, $z \gg 0$, the half-angle beam divergence can be expressed as

$$\theta = \frac{\omega(z)}{z}. \tag{5.2}$$

By using (2.9) and (2.10), (5.2) can be written as

$$\theta = \frac{\lambda}{\pi\omega_0}M^2, \tag{5.3}$$

and by relating θ to the NA with (2.3), and the fact that at the beam waist, ω_0, is the radius of the fiber core, r_c,

$$M^2 = \frac{\pi r_c}{\lambda}NA \tag{5.4}$$

is obtained and can be used to estimate the M^2-factor for an optical fiber. According to (5.3), the ratio between the half-angle beam divergence, θ, and the M^2-factor is constant. Therefore the M^2-factor limits the degree to which the beam can be focused, for a given θ, which is given and limited by the NA of the focusing lens. The M^2-factor also, together with the optical power, determines the laser beam radiance.

Knife Edge Technique

When the beam width is measured with the knife edge technique it is often the beam radius, ω, rather than the beam diameter, D_{L}, which is measured at the $\frac{1}{e^2}$ peak of irradiance points. Therefore (2.11) has to be expressed with ω, and for a Gaussian beam, the relation between ω and D_{L} is $D_{\mathrm{L}}^2 = 2\omega^2$ [35]. Equations (2.14) and (2.15) are then transformed to

$$E_0 = \frac{2\Phi_0}{\pi\omega^2}, \tag{5.5}$$

and

$$\Phi_0 = \frac{\pi E_0 \omega^2}{2}, \tag{5.6}$$

respectively.

Equation (2.15) can be rewritten with Cartesian coordinates, and assuming that $y = 0$, x can be substituted for ρ. This gives the local irradiance in the x-direction, where x is the distance from the center of the beam;

$$E = E_0 \exp\left(-\frac{2x^2}{\omega^2}\right). \tag{5.7}$$

In the same manner the local irradiance in the y-direction can be found by assuming $x = 0$, and by combining the two dimensions the local irradiance can be expressed as

$$E = E_0 \exp\left(-\frac{2x^2 + 2y^2}{\omega^2}\right), \tag{5.8}$$

and hence the total power in the beam is

$$\Phi_0 = \int_{-\infty}^{\infty}\int_{-\infty}^{\infty} E_0 \exp\left(-\frac{2x^2 + 2y^2}{\omega^2}\right) \mathrm{d}x\,\mathrm{d}y. \tag{5.9}$$

To solve this double integral, the following substitution can be used;

$$\begin{aligned} t &= \frac{y}{\omega} \Rightarrow \mathrm{d}t = \frac{\mathrm{d}y}{\omega}, \\ u &= \frac{x}{\omega} \Rightarrow \mathrm{d}u = \frac{\mathrm{d}x}{\omega}, \end{aligned} \tag{5.10}$$

as well as the standard integral

$$\int_{-\infty}^{\infty} \exp\left(-at^2\right)\, \mathrm{d}t = \sqrt{\frac{\pi}{a}}. \tag{5.11}$$

Computation yields

$$\Phi_0 = \frac{E_0 \pi \omega^2}{2}, \tag{5.12}$$

which is in agreement with (5.6).

If the knife edge now is allowed to block a certain part of the beam, the total power would be

$$\Phi_0 = \int_{-\infty}^{\infty} \int_{-\infty}^{P} E_0 \exp\left(-\frac{2x^2 + 2y^2}{\omega^2}\right)\, \mathrm{d}x\, \mathrm{d}y, \tag{5.13}$$

where P is the location where the knife edge is placed. The integral in respect of y can be solved, but in respect of x the integral can not be solved in closed form. To solve in respect of x, the error function has to be introduced;

$$\mathrm{erf}(X) = \frac{2}{\sqrt{\pi}} \int_0^X \exp\left(-t^2\right) \mathrm{d}t, \tag{5.14}$$

which is tabulated in scientific handbooks. In order to use the error function, the following substitution has to be used;

$$t = \frac{\sqrt{2}(x - x_0)}{\omega} \Rightarrow \mathrm{d}t = \frac{\sqrt{2}\mathrm{d}x}{\omega}, \tag{5.15}$$

where x_0 is the central position of the Gaussian beam.

It is now possible to describe the total beam power in the x-direction as

$$\Phi_x = \Phi_0 \left[0.5 + 0.5 \cdot \mathrm{erf}\left(\frac{\sqrt{2}\,(x - x_0)}{\omega}\right)\right], \tag{5.16}$$

where x represents a point after the beam center where the knife edge is placed. Notice that if $x \to \infty$ (the knife edge is removed from the beam), then $\Phi_x = \Phi_0$ since $erf(\infty) = 1$, which is physically correct. The definition of the beam width

will, during this thesis, be the distance between $x_{10\%}$ and $x_{90\%}$, see figure 5.5, and this yields the following system;

$$\begin{cases} \Phi_{10\%} = \Phi_0 \left[0.5 + 0.5 \cdot \text{erf}\left(\frac{\sqrt{2}(x_{10\%} - x_0)}{\omega}\right)\right] \\ \Phi_{90\%} = \Phi_0 \left[0.5 + 0.5 \cdot \text{erf}\left(\frac{\sqrt{2}(x_{90\%} - x_0)}{\omega}\right)\right] \end{cases} . \tag{5.17}$$

Since this system has two equations and two unknown variables, ω can be found.

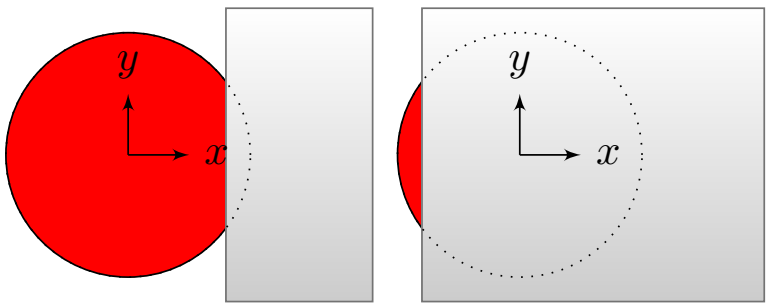

Figure 5.5: The knife edge is used to block 10% and 90% of the beam, in this case in the $x-$direction.

x_0 is expressed from the top equation of (5.17), and used in the lower equation of (5.17). This gives

$$\begin{aligned} \omega &= \frac{\sqrt{2}}{\text{erf}^{-1}\left(\frac{4}{5}\right) - \text{erf}^{-1}\left(\frac{-4}{5}\right)} (x_{90\%} - x_{10\%}) \approx \\ &\approx \frac{(x_{90\%} - x_{10\%})}{1.28}. \end{aligned} \tag{5.18}$$

Setup of M^2 measurements

The beam quality factor, M^2, was measured with the $10\%-90\%$ knife edge technique described above. In order to measure the beam radius with this technique, the collimated output was focused with a 300 mm lens, placed after the mirror M2. A translation stage mounted with razor edges was placed after the lens, and a power meter measured the output.

Experiments gave an M^2-factor of 1.05 and 1.02 in the $x-$ and $y-$direction, respectively. These values are expected since the output is SM, and the data fitted to (2.9) can be seen in figure 5.6. The beam waist was according to the fit 74.5 μm and 73.1 μm in the $x-$ and $y-$direction, respectively, while theoretical calculations

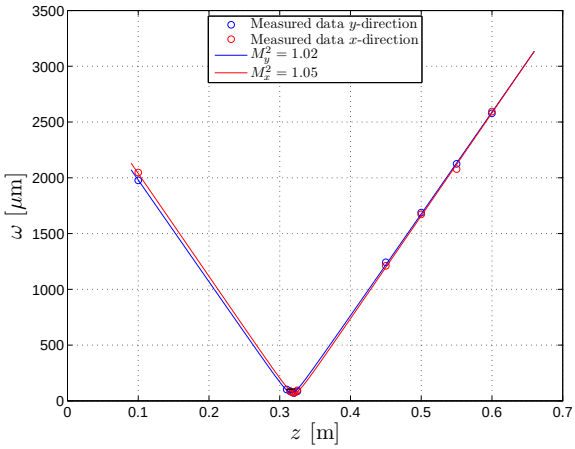

Figure 5.6: The M^2 fit with measured data points, obtained via the $10\% - 90\%$ knife edge technique.

and simulations gave 50 μm in each direction. The Rayleigh range was measured to be 105 μm and 103 μm in the $x-$ and $y-$direction, respectively. The intensity profile, before the collimating lens, was measured with a Pyrocam, and confirmed SM-operation and is illustrated in figure 5.7.

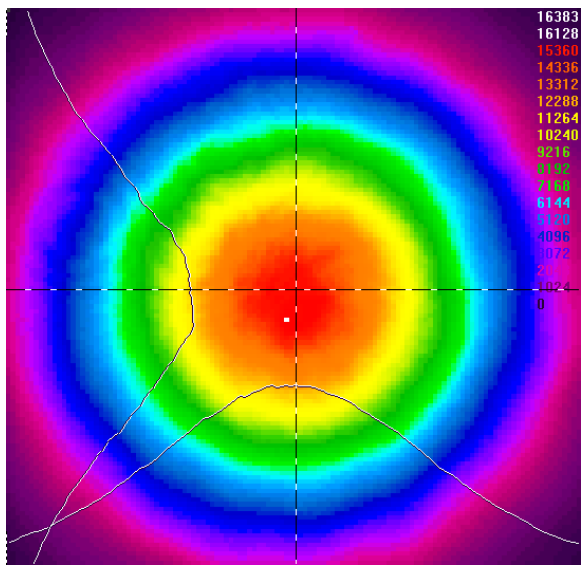

Figure 5.7: The intensity profile of the signal before the collimating lens.

Chapter 6

Discussion

In this chapter the previously presented results are discussed and analyzed, and a few obstacles are also discussed.

6.1 Simulations

Simulations of the gain at maximum available pumping power also showed that a fiber length of 3 m was optimum. Figure 6.1 shows how the gain of the fiber alters,

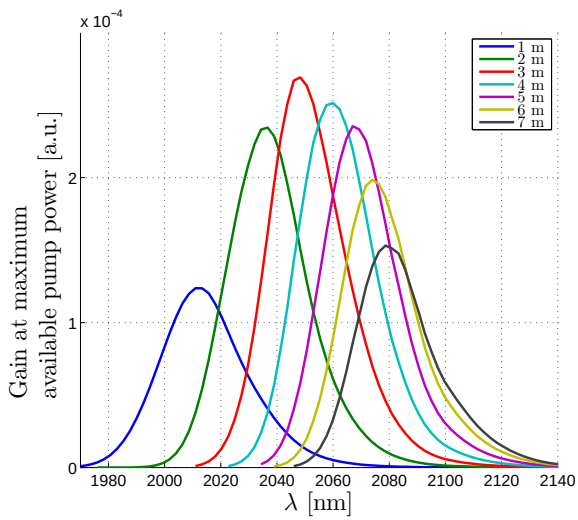

Figure 6.1: Simulations of the gain with respect to different fiber lengths.

as the fiber length is varied. At short lengths, not all pump power will be absorbed. According to simulations the highest gain was obtained with a fiber length of 3 m, and thereafter the gain decreased, due to reabsorption and pump energy converted into thermal energy. The wavelength clearly increases with increasing fiber length, and this is also due to reabsorbtion in the fiber.

According to simulations, the optimum fiber length, with respect to output power, was about 3.5 meters. As the losses were increased, the optimum length was shifted towards shorter cavity lengths. Therefore a shorter cavity length of 3 meters was chosen, also to suppress self pulsing within the cavity. If the cavity, i.e. the active fiber, is shorter there is less chance of under pumping. The pump light will be absorbed in the active fiber, and therefore there is only a small amount of pump in the end of the fiber. Otherwise reabsorption of the signal may be introduced, which will initiate saturable absorber properties, and therefore enhance the risk of self pulsing. One way to suppress the self pulsing due to reabsorption is to dual pump the fiber, i.e. pump the fiber from both ends.

Table 6.1: Parameters to simulate the thulium fiber laser.

Parameter	Value	Description
τ_{21}	0.66 [ms]	Lifetime of the upper laser level $^3F4$
η_{CR}	55%	CR efficiency
λ_{p}	$2 \cdot 793 \cdot \eta_{\mathrm{CR}}$ [nm]	Pump wavelength adjusted for the CR efficiency
$\sigma_{12,\mathrm{p}}$	$4.5 \cdot 10^{-25}$ [m^2]	Absorption cross-section of Tm-doped Si-fibers at the pump wavelength, data from [16]
$\sigma_{21,\mathrm{p}}$	$3.9 \cdot 10^{-25}$ [m^2]	Emission cross-section of Tm-doped Si-fibers at the pump wavelength, data from [16]
$\eta_{i,\mathrm{p}}$	10%	Incoupling loss of the pump (splicing losses)
P_{p}	$3.26 \cdot \eta_{i,\mathrm{p}}$ [W]	Pump power adjusted for incoupling losses
L	2.8 [m]	Length of the active Tm-fiber
A_{core}	$\pi {r_{\mathrm{c}}}^2$ [m^2]	Core area
A_{cladding}	πr_{cl}^2 [m^2]	Cladding area
α_{dB}	3 [dB/m]	Cladding absorption at λ_{p}, provided by Nufern
R_0	99%	Reflectivity of input-coupler at $\lambda \geq 2050$ nm
R_{L}	3.84%	Reflectivity of output-coupler
A_0	5%	Losses of input-coupler

A counter-propagating setup provides the highest output power [6], but since simulations showed that the output power only was sufficiently smaller for the co-propagating setup, the latter was chosen. The physical reasoning for this is that the pump signal is strongest in the same region where the signal is strongest. Therefore, the signal will deplete the inversion, rather than the ASE [36].

Experimental data presented in the previous chapter was consistent with simulated values. For instance the residual pump was, according to the model -8.2 dB, while measured values were -6.8 dB, -8.4 dB, -10.7 dB, and -12.4 dB, corresponding to coiling diameters of $\phi = 30$, 15, 7.5, and 3.5 cm. The output powers, depending on ϕ, were 0.62 W, 0.7 W, 0.79 W, and 0.86 W, cycling from $\phi = 30$ cm to $\phi = 3.5$ cm. The simulated output was 0.86 W. Parameters used during simulations are presented in table 6.1.

6.2 Pump diode characterization

The characterization of the pump diode was consistent with the data-sheet of the diode, provided by Oclaro, with a maximum output power of 3.26 W. The cladding absorption at the pump wavelength in the active Tm-fiber was given as 3 dB/m, and according to the Beer-Lambert law the absorption can be given as [37]

$$\alpha_{\mathrm{dB}} = -\frac{10}{L}\log\left(\frac{P_{\mathrm{out}}}{P_{\mathrm{in}}}\right), \tag{6.1}$$

where α_{dB} is the cladding absorption given in [dB/m], and L the fiber length. If the ratio between the input and output power is expressed as a function of L,

$$\frac{P_{\mathrm{out}}}{P_{\mathrm{in}}} = 10^{-\frac{\alpha_{\mathrm{dB}}L}{10}}, \tag{6.2}$$

is obtained. This equation does however not account for different kind of losses, i.e. bending losses.

If $L = 0$, all of the input power will obviously propagate to the power meter. Although, as the length of the fiber increases, more power is absorbed. The theoretical and measured absorption are shown in figure 6.2. Examining the plot shows that the absorbed pump power increases with decreasing ϕ. This is due to bending losses, and that more pump light is forced into the core at harder coiling.

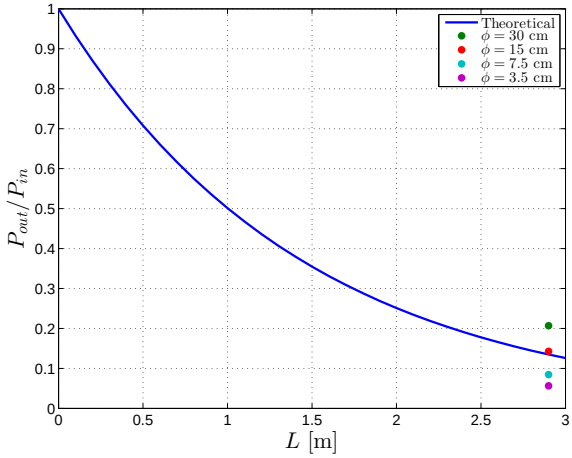

Figure 6.2: The absorption ratio versus fiber length, at maximum pump power.

6.3 Thulium fiber laser characterization

The laser efficiency is an important consideration with regards to development of the laser. It depends primarily on the length of the active fiber and the fiber coiling diameter, and of course the pump wavelength.

The maximum output power, obtained at a coiling diameter of 3.5 cm, was 0.86 W. The highest slope efficiency and CR efficiency were also obtained with ϕ= 3.5 cm, 47% and 61% respectively. The lowest power threshold, 1.12 W, was on the other hand obtained with ϕ= 30 cm.

6.3.1 Power measurements

As mentioned earlier, tighter coiling of the active fiber induces bending losses, and more pump light is forced into the core. Therefore η_s increases at smaller ϕ, and since η_{CR} relates linearly to η_s according to (3.1), η_{CR} also increases. The data from table 5.2 is plotted in figures 6.3 and 6.4. The slope efficiency appears to decrease with increasing ϕ, but increases again at $\phi = 15$ cm. The maximum and threshold power decrease with increasing bending radii. This is due to, which has been mentioned earlier, less absorption of the pump light. According to McComb [13], a coiling of about 10 cm will introduce significant differential losses between the fundamental mode and the next highest order mode. McComb claims this is an

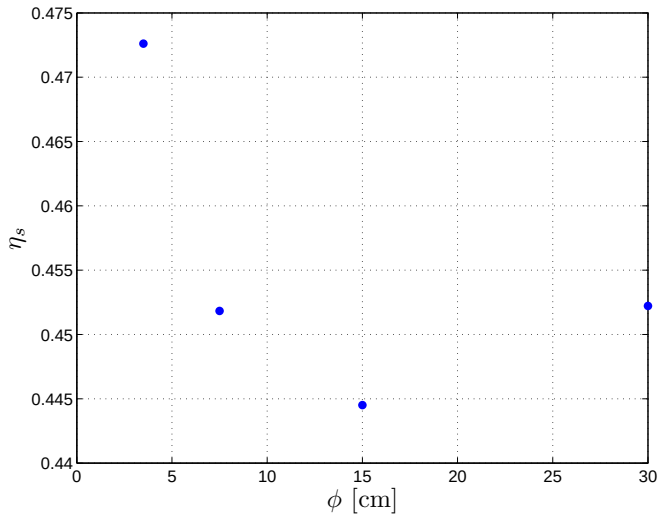

Figure 6.3: The slope efficiency, η_s, versus the coiling diameter, ϕ, of the active thulium fiber.

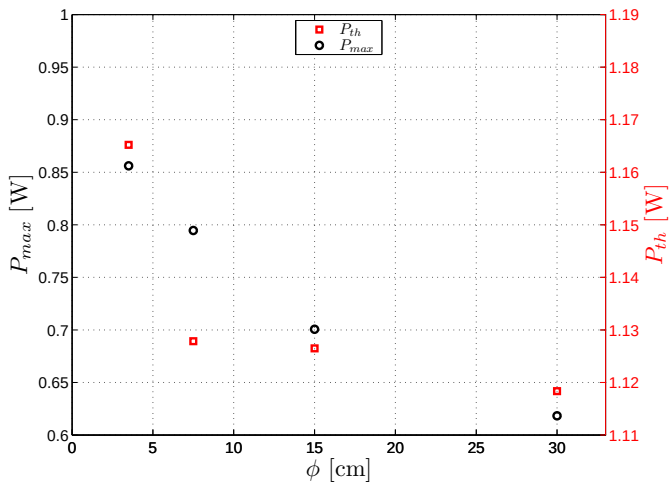

Figure 6.4: The maximum output power, $P_{\max}$ (black circles, left y-axes), and the threshold power, P_{th} (red squares, right y-axes), versus the coiling diameter of the active thulium fiber.

important aspect of maintaining SM beam quality. Compared to Yb, Tm can, due to its larger NA, be bent up to 25% tighter with minimal loss. Although, as the fiber core diameter increases, the fiber's sensitivity to bending increases.

6.3.2 Spectral characterization

The optical spectrum of the output signal can be seen in figure 5.3. If the data is examined in more detail, it can be seen that the peak is at 2051 nm, although the FBG is HR at 2050 nm. The shift in wavelength is probably, as Pask *et al* claims,

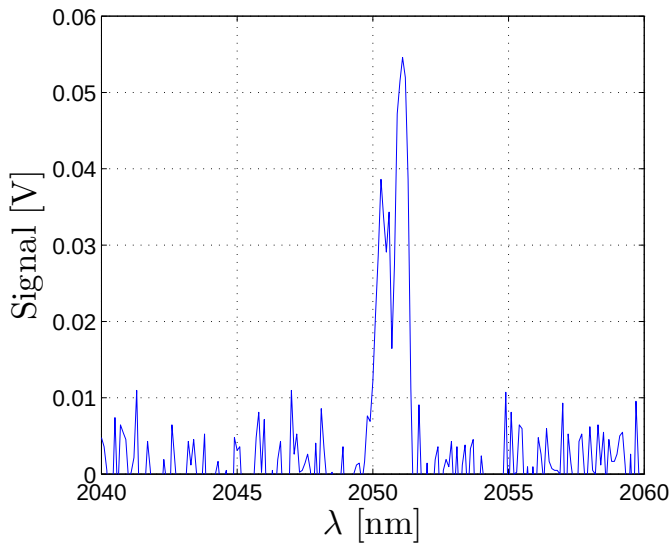

Figure 6.5: The spectral output of the thulium fiber laser.

due to reabsorption in the length of the fiber [38]. However, Pask *et al* also states that the gain maximum moves progressively to shorter wavelengths as the pump power increases. Also, the FBG has a temperature dependency, according to (3.15), which may contribute to the wavelength shift.

By examining the peak in figure 5.3, one finds that it is actually not one peak, but two, by scanning over a smaller wavelength range, see figure 6.5. This may be due to self-pulsing, introduced by reabsorption mentioned earlier. It could also be atmospheric absorption. However, one must remember that the resolution was 5.5 nm, and therefore one should be careful to not rush to conclusions.

6.3.3 Spatial characterization

An M^2 value of 1.05 and 1.02 was measured in the $x-$ and $y-$direction, respectively. Such a good M^2 is expected since the core diameter yields a V-parameter, see (2.8), smaller than 2.405 and thus gives a SM output. An approximation of M^2 can be estimated through (5.4), which gives an M^2 of 1.15. An even more accurate approximation is to use Marcuse's equation to calculate the mode radius, and use instead of the core radius. Marcuse's equation is

$$\frac{\omega}{r_c} \approx 0.65 + \frac{1.619}{V_{nr}^{3/2}} + \frac{2.879}{V_{nr}^{6}}. \tag{6.3}$$

Solving for ω, and inserting data gives $\omega \approx 5.67\,\mu$m, which in turn gives an estimated value of $M^2 = 1.3$.

The beam waist was measured to be about 75 and 73 μm in the x- and y-direction. A theoretical approach to calculate the beam waist, with (2.9) and (D.16), gave 49 and 48 μm in respective direction, which corresponds well with the Winlase simulation of 50 μm. The difference between the simulated/theoretical beam waist and the actual beam waist, was probably due to the fact that the beam was not perfectly collimated.

The M^2 was measured with the setup described in 5.1.4, but other setups were tested before. The obtained M^2 was then 4-5, or the physical impossible value of $M^2 < 1$. The reason for the poor values was the collimating lens. The collimating lens had an anti-reflection (AR) coating at a different wavelength than the pump or signal, and this introduced aberrations. The intensity profile was not Gaussian at all, and resembled a heavily diffracted beam, see figure 6.6. The aberrations were probably introduced due to a Fabry-Perot interferometer, created between the surfaces of the AR-coating and the lens. This kind of interferometer is created by the multiple reflections of two closely spaced semi-transparent surfaces. Each time the beam reaches the second surface, part of the light is transmitted which creates multiple offset beams that interfere with each other. This kind of interferometer has a high resolution due to the large amount of interfering rays, and the condition for each maxima follows the interference condition for thin films,

$$2d\cos\alpha = m\lambda, \tag{6.4}$$

where d is the distance between the semi-transparent surfaces, and m is the order of interference, increasing towards the center. At small angles, the interference

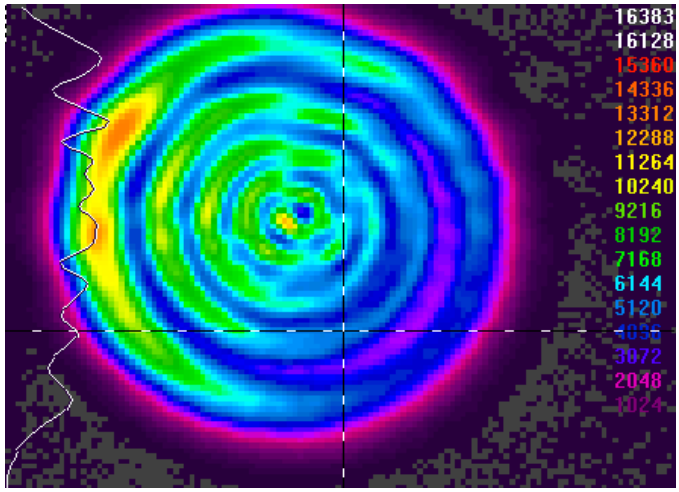

Figure 6.6: The intensity profile of the signal indicating interference effects introduced by the collimating lens.

condition can be approximated as $2d \approx m\lambda$. Solving for d gives the thickness of the AR-coating to be around 4-5 μm.

Chapter 7

Conclusion

The aim of this project, to develop a stable narrow linewidth all-fiber cavity TFL, was successfully met, with an output power of 0.86 W at 2051 nm, with a FWHM of 1.5 nm, excellent beam quality, $M^2 \leq 1.05$ in both directions, and a slope efficiency of 47%. It was realized with an all-fiber cavity consisting of a HR FBG and the Fresnel reflection of a perpendicular cleaved fiber end, where the Fresnel reflection acted as the output coupler. The active fiber was cladding pumped with the help of a commercial LD at 793 nm.

Several parameters (η_s, P_{max} and P_{th}) behaviour were investigated depending on the coiling diameter, ϕ, of the active Tm-fiber. The slope efficiency decreased as the coiling diameter increased, with a maximum at $\phi = 3.5$ cm and minimum at $\phi = 15$ cm, while the output power with respect to the absorbed pump power, displayed a linear trend. The maximum output power and threshold power decreased with increasing ϕ. A harder coiling introduces losses of higher order modes, and forces the pump light into the core, thus increasing the absorption.

The spectral output was at 2051 nm with a FWHM of 1.5 nm, even though the design wavelength of the FBG was 2050 nm. This might be explained by reabsorption in the fiber [38], or the temperature dependency a FBG has [31].

7.1 Suggested improvements and future work

The concentration of Tm ions in the active fiber was 1 mol%, and according to Jackson [19] and McComb [13], the slope efficiency and the overall CR operation

increase with increasing Tm concentration. In order to optimize the slope efficiency an active fiber with higher dopant concentration of Tm could be used. McComb claims that a doping concentration of 2-5 wt% is necessary to achieve an efficient CR-process. Although an exaggerated Tm concentration will lead to a poor η_s, due to inter-ion effects, i.e. upconversion and reabsorption, will dominate because of clustered Tm-ions. Al-ions can be introduced to enhance the solubility of Tm-ions in the glass [13].

According to Richardson *et al*, the route which offers the highest power levels are in-band pumping with multiple high power Er-fiber lasers at ~1600 nm [3]. This approach is however not as simple and cheap as pumping with commercial diodes, such as AlGaAs, at ~800 nm. Another type of pump scheme, which would lead to a 5-dB gain improvement of pump absorption and better power conversion efficiency compared to single end pumping according to Roy *et al* [39], is bidirectional pumping. Bidirectional pumping is a type of dual pumping.

Better lab equipment is always an option, for instance a collimating lens suited for 2 μm operation. A dry-air box could be used to avoid atmospheric absorption, which may interfere with the spectral measurements. A cooling system could be implemented to increase η_s, although the current pump diode was restricted to relatively low powers (max 3.26 W). Although the splice losses were low, there is always room for improvement, and lower splice losses would increase the laser properties in form of better η_s, higher pump powers, and therefore also higher output powers.

The TFL developed during this thesis project could be used as a seed source, creating a MOFA scheme. The laser could also be mode-locked, by splicing a passive carbon nanotube doped fiber to the active fiber. Although, this would remove the output coupler (Fresnel reflection from the fiber end). However, a 12% reflectivity FBG was bought from TeraXion together with the HR FBG used as input coupler, and the 12% FBG could be used as output coupler. The output would practically be the same, although simulations showed a slight decrease of output power.

Ho is a RE-element with an emission span at slightly higher wavelengths than Tm. These wavelengths are inaccessible for Tm due to the diminishing emission cross-section of Tm in Si-fibers [40]. If the HR FBG was reflective at 1950 nm (which actually were bought), instead of 2050 nm, the TFL could be used to pump a Ho fiber laser.

Bibliography

[1] K. C. Kao and G. A. Hockham, "Dielectric-fibre surface waveguides for optical frequencies," *IEE Proceedings, J Optoelectronics*, vol. 113, no. 7, pp. 191–198, 1986.

[2] R. J. Mears, L. Reekie, I. M. Jauncey, and D. N. Payne, "Low-noise erbium-doped fibre amplifier operating at 1.54 μm," *Electronics Letters*, 1987.

[3] D. J. Richardson, J. Nilsson, and W. A. Clarkson, "High power fiber lasers: current status and future perspectives," *Optical Society of America*, vol. 27, no. 11, pp. B63–B91, 2010.

[4] E. Stiles, "New developments in ipg fiber laser technology," in *Proceedings of the 5th International Workshop on Fiber Lasers.*

[5] S. D. Jackson, "Yb-doped silica fiber lasers: Versatile sources for the 1-1.2 μm region," *Optics Communications*, 2003.

[6] Y. Tang, C. Huang, S. Wang, H. Li, and J. Xu, "High-power narrow-bandwidth thulium fiber laser with an all-fiber cavity," *Optics Express*, vol. 20, no. 16, pp. 17539–17544, 2012.

[7] T. Ehrenreich, R. Leveille, I. Majid, K. Tankala, G. Rines, and P. Moulton, "1-kw, all-glass tm:fiber laser," in *SPIE Photonics West 2010: LASE, Fiber Lasers VII: Technology, Systems, and Applications, Conference 7580.*

[8] S. Ishii, K. Mizutani, H. Fukuoka, T. Ishikawa, B. Philippe, H. Iwai, T. Aoki, T. Itabe, A. Sato, and K. Asai, "Yb-doped silica fiber lasers: Versatile sources for the 1-1.2 μm region," *Optics Communications*, 2010.

[9] G. Renz and W. Bohn, "Two-micron thulium-pumped-holmium laser source for dircm applications," 2007.

[10] P. Jelger, *High Performance Fiber Lasers With Spectral, Thermal and Lifetime Control*. PhD thesis, Royal Institute of Technology, 2009.

[11] E. Hecht, *Optics*. Addison-Wesley, 2001.

[12] J. P. Koplow, D. A. V. Kliner, and L. Goldberg, "Single-mode operation of a coiled multimode fiber amplifier," *Optics Letters*, vol. 25, pp. 442–444, 2000.

[13] T. S. McComb, *Power Scaling of Large Mode Area Thulium Fiber Lasers in Various Spectral and Temporal Regimes*. PhD thesis, University of Central Florida, 2009.

[14] J. Nilsson*, W. Clarkson, R. Selvas, J. Sahu, P. Turner, S.-U. Alam, and A. Grudininb, "High-power wavelength-tunable cladding-pumped rare-earth-doped silica fiber lasers," *Optical Fiber Technology*, 2004.

[15] P. Zhao, J. Liu, C. Zhao*, H. Yang, and J. Wen, "The slope efficiency of 2 μm thulium doped fiber laser," *High-Power Lasers and Applications V*, 2010.

[16] S. Agger and J. H. Povlsen, "Single-mode operation of a coiled multimode fiber amplifier," *Optics Letters*, vol. 29, no. 11, pp. 1503–1505, 2004.

[17] O. Svelto, *Principles of Lasers*. Springer, 1976.

[18] J. Geng, J. Wu, S. Jiang, and J. Yu, "Efficient operation of diode-pumped single-frequency thulium-doped fiber lasers near 2 μm," *Opt. Lett.*, vol. 32, pp. 355–357, Feb 2007.

[19] S. D. Jackson, "Cross relaxation and energy transfer upconversion processes relevant to the functioning of 2 μm tm^{3+}-doped silica fibre lasers," *Optics Communications*, 2004.

[20] P. F. Moulton, G. A. Rines, E. V. Slobodtchikov, K. F. Wall, G. Frith, B. Samson, and A. L. G. Carter, "Tm-doped fiber lasers: fundamentals and power scaling," *IEEE J. Sel. Top. Quant. Electron*, vol. 15, pp. 85–92, 2009.

[21] S. D. Jackson and T. A. King, "Theoretical modeling of tm-doped silica fiber lasers," *Journal of Lightwave Technology*, vol. 17, no. 5, pp. 948–956, 1999.

[22] C. R. Giles and E. Desurvire, "Theoretical modeling of fiber laser at 810 nm based on thulium-doped silica fibers with enhanced $^3h_4$ level lifetime," *Optical Society of America*, vol. 19, no. 3, pp. 2773–2781, 2011.

[23] K. O. Hill and G. Meltz, "Fiber bragg grating technology fundamentals and overview," *Journal of lightwave technology*, 1997.

[24] D. K. W. Lam and B. K. Garside, "Characterization of single-mode optical fiber filters," *Applied Optics*, 1981.

[25] G. Meltz, W. W. Morey, and W. H. Glenn, "Formation of bragg gratings in optical fibers by a transverse holographic method," *Optics Letters*, 1989.

[26] Z. Yu, *Fibre Bragg Grating Components for Filtering, Switching and Lasing*. PhD thesis, Royal Institute of Technology, 2008.

[27] R. Paschotta, "Fiber bragg gratings." Internet. http://www.rp-photonics.com/fiber_bragg_gratings.html.

[28] T. Erdogan, "Fiber grating spectra," *Journal of Lightwave Technology*, vol. 15, no. 8, pp. 1277–1294, 1997.

[29] P. Rugeland, *Applications of monolithic fiber interferometers and actively controlled fibers*. PhD thesis, Royal Institute of Technology, 2013.

[30] H. Kogelnik, "Theory of optical waveguides," *Guided-Wave Optoelectronics*, 1990.

[31] Y. Kondo, K. Nouchi, T. Mitsuyu, M. Watanabe, P. G. Kazansky, and K. Hirao, "Fabrication of long-period fiber gratings by focused irradiation of infrared femtosecond laser pulses," *Optics Letters*, 1999.

[32] A. Martinez, I. Y. Khrushchev, and I. Bennion, "Thermal properties of fibre bragg gratings inscribed point-by-point by infrared femtosecond laser," *Electronics Letters*, 2005.

[33] C. R. Giles and E. Desurvire, "Modeling erbium-doped fiber amplifiers," *Journal of Lightwave Technology*, vol. 9, pp. 271–283, 1991.

[34] P. Zeil* and F. Laurell, "On the tunability of a narrow-linewidth yb-fiber laser from three- to four-level lasing behaviour," *Optical Society of America*, 2011.

[35] W. J. Marshall, "Two methods for measuring laser beam diameter," *Journal of Laser Applications*, 2010.

[36] P. M. Becker, A. A. Olsson, and J. R. Simpson, *Erbium-Doped Fiber Amplifiers: Fundamentals and Technology.* Academic Press, 1999.

[37] G. P. Agrawal, *Nonlinear Fiber Optics.* Academic Press, 2001.

[38] H. M. Pask, R. J. Carman, D. C. Hanna, A. C. Tropper, C. J. Mackechnie, P. R. Barber, and J. M. Dawes, "Yb-doped silica fiber lasers: Versatile sources for the 1-1.2 μm region," *IEEE Journal of Selected Topics in Quantum Electronics*, 1995.

[39] F. Roy, D. Bayart, and P. Bianiel, "Optical fiber communication conference," in *Novel pumping schemes for thulium doped fiber amplifier.*

[40] N. Simakov*, A. Hemming, W. A. Clarkson, J. Haub, and A. Carter, "A cladding-pumped, tunable holmium doped fiber laser," *Optical Society of America*, 2013.

[41] F. Knappe, *Waveguide structuring and Bragg grating fabrication by UV light induced refractive index changes in photosensitive optical materials.* Cuvillier Verlag, 2007.

[42] M. Fokine, *Photosensitivity, chemical composition gratings, and optical fiber based components.* PhD thesis, Royal Institute of Technology, 2002.

[43] A. Martinez, M. Dubov, I. Y. Khrushchev, and I. Bennion, "Direct writing of fibre bragg gratings by femtosecond lasers," *Electronics Letters*, 2004.

[44] E. Wikszak, J. Burghoff, M. will, S. Nolte, A. Tünnermann, and T. Gabler, "Recording of fiber bragg gratings with femtosecond pulses using a point by point technique," *Conference on Lasers and Electro-Optics*, 2004.

[45] T. Geernaert, K. Kalli, C. Koutsides, M. Komodromos, T. Nasilowski, W. Urbanczyk, J. Wojcik, F. Berghmans, and H. Thienpont, "Point-by-point fiber bragg grating inscription in free-standing step-index and photonic crystal fibers using near-ir femtosecond laser," *Optics Letters*, 2010.

[46] J. Thomas, E. Wikszak, T. Clausnitzer, U. Fuchs, U. Zeitner, S. Nolte, and A. Tünnermann, "Inscription of fiber bragg gratings with femtosecond pulses using a phase mask scanning technique," *Applied Physics A*, 2007.

Appendix A

Photosensitivity

Photosensitivity

The physics behind photosensitivity is still being researched, and according to Knappe [41] this is due to the fact that the photosensitivity response will differ depending on several factors, such as the type of fiber, writing wavelength and the laser power. The main models for photosensitivity are however the following;

a) Color-center model

b) Stress relaxation model

c) Densification-compaction model.

The color-center model claims that the color-center[1] related changes in the UV-absorption are related to the refractive index through the Kramers-Kronig relations. The core is irradiated at a certain wavelength which induces a bleaching at the corresponding wavelength band, and creates a growth of absorption bands located at a slightly different wavelength.

The stress relaxation model explains photosensitivity through stress-opto effects. Different manufacturing techniques and material properties may introduce stressed regions in an optical fiber, and the relaxation of stress will induce a change in the refractive index. The difference in thermal expansion coefficient, between the core and the cladding, will create residual stress as the fiber cools (after manufacturing).

[1] The color-center is absoprtion peaks in the UV-range.

Thermoelastic stress occurs from the fact that the core and the cladding have different transition temperatures. The last stress, mechanical stress, arises when the fiber is extracted from the drawing furnace. UV induced stress relaxation may not be a mechanism involved in photosensitivity, this is however beyond the scope of this master thesis.

The last model, the densification-compaction model, explains the photosensitivity phenomenon by claiming that irradiation promotes compaction/density changes in the glass matrix. This is a known fact since it has been observed through atomic force microscopy (AFM), transmission electron microscopy (TEM), Raman spectra and changes in the core tension. Changes in the core tension are correlated to a change in the refractive index, and thus indicating photosensitivity [42].

Appendix B

Pump Diode, additional plots

The stability of the pump diode is illustrated in figure B.1. The R_{NTC} was kept constant, and therefore the pump wavelength altered, as the temperature increased.

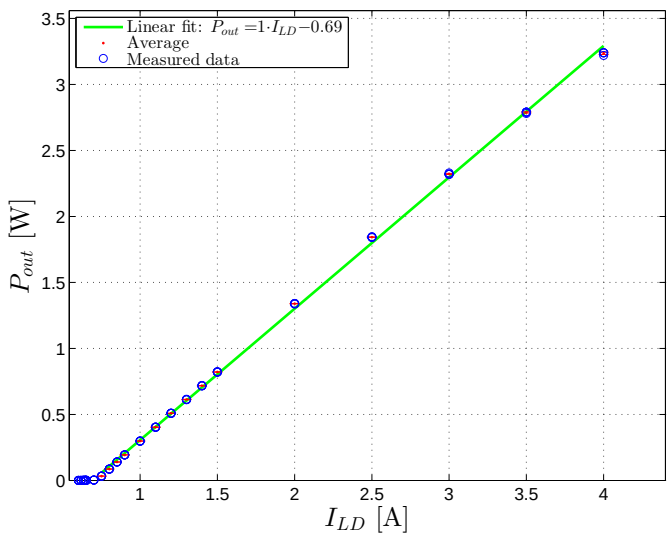

Figure B.1: Laser diode output power as a function of the diode current.

Figure B.2 shows how the temperature depend on the pump power, at a pump wavelength of 793.0 ± 0.1 nm.

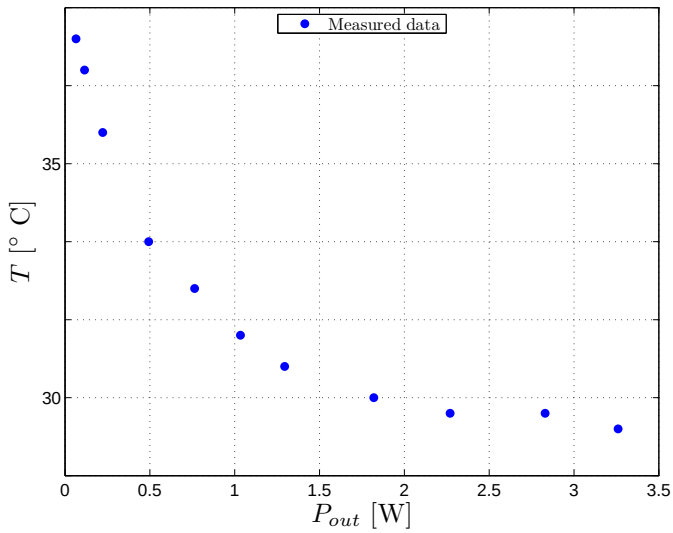

Figure B.2: The temperature of the Peltier element versus the output power of the laser diode at 793.0 ± 0.1 nm.

Appendix C

Thulium Fiber Laser, additional plots

The laser characterization was made with respect to input and absorbed pump power. The coiling diameter, ϕ, was also used as a variable. Below follows all relevant plots.

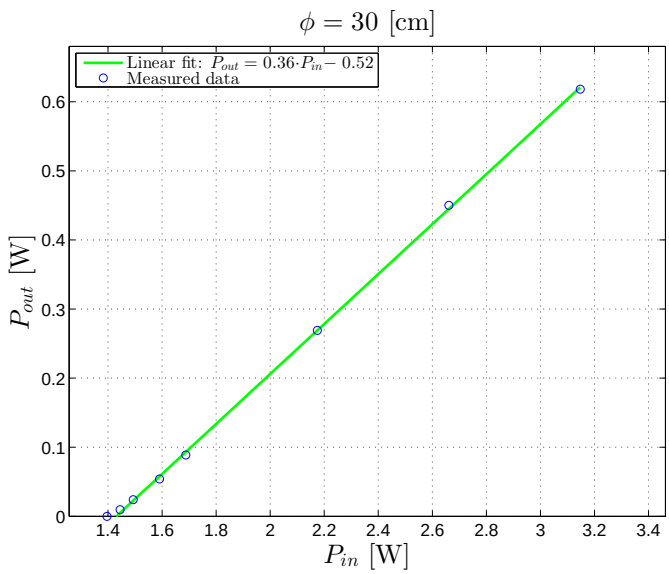

Figure C.1: Output power versus pump power, at a coiling diameter of 30 cm.

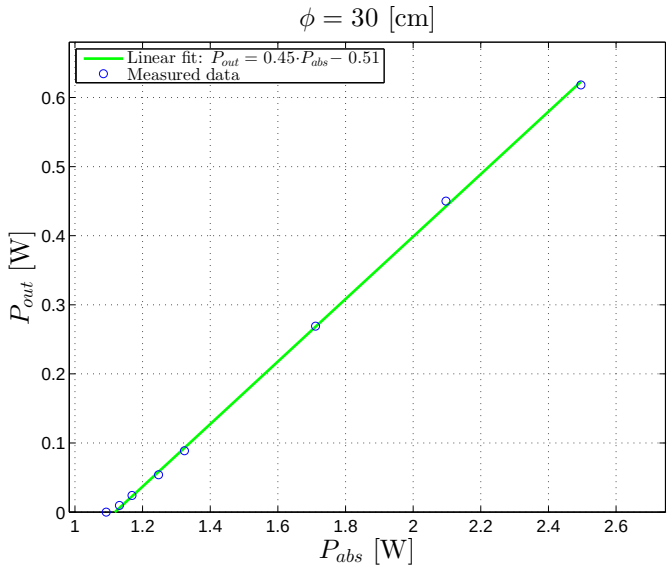

Figure C.2: Output power versus absorbed pump power, at a coiling diameter of 30 cm.

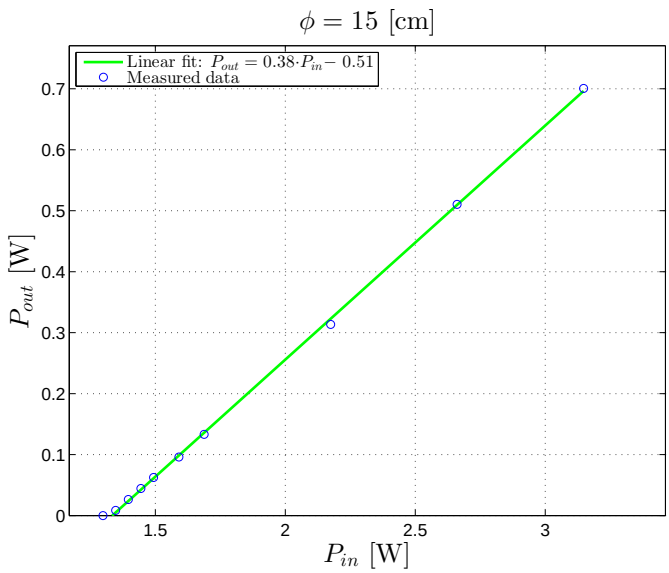

Figure C.3: Output power versus pump power, at a coiling diameter of 15 cm.

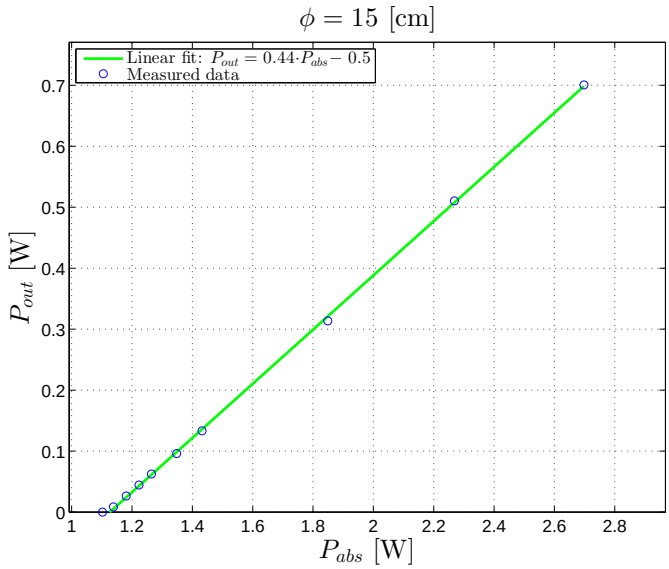

Figure C.4: Output power versus absorbed pump power, at a coiling diameter of 15 cm.

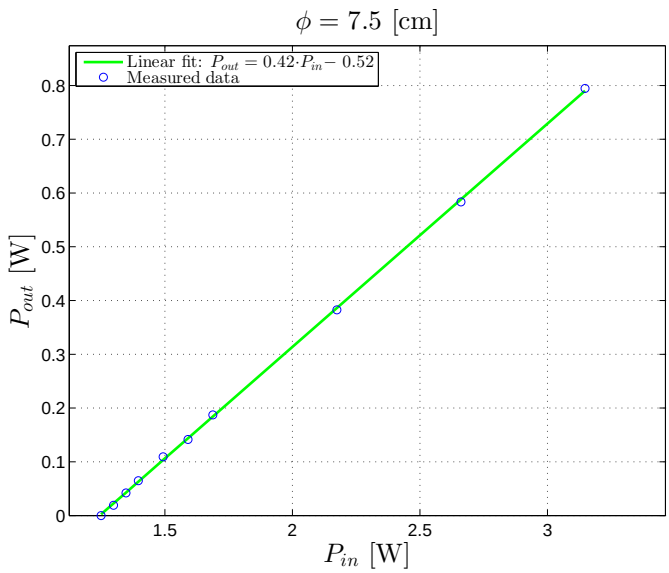

Figure C.5: Output power versus pump power, at a coiling diameter of 7.5 cm.

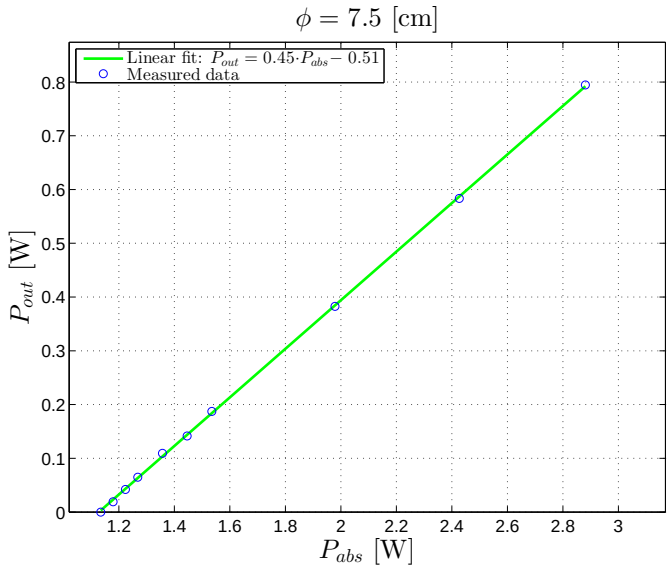

Figure C.6: Output power versus absorbed pump power, at a coiling diameter of 7.5 cm.

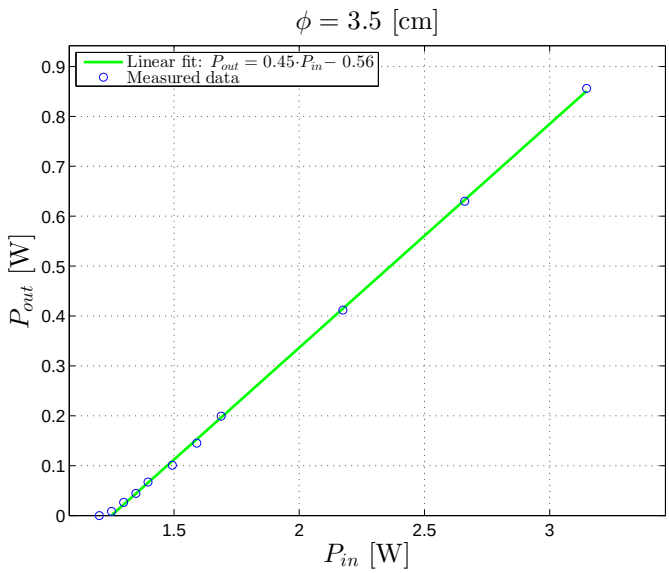

Figure C.7: Output power versus pump power, at a coiling diameter of 3.5 cm.

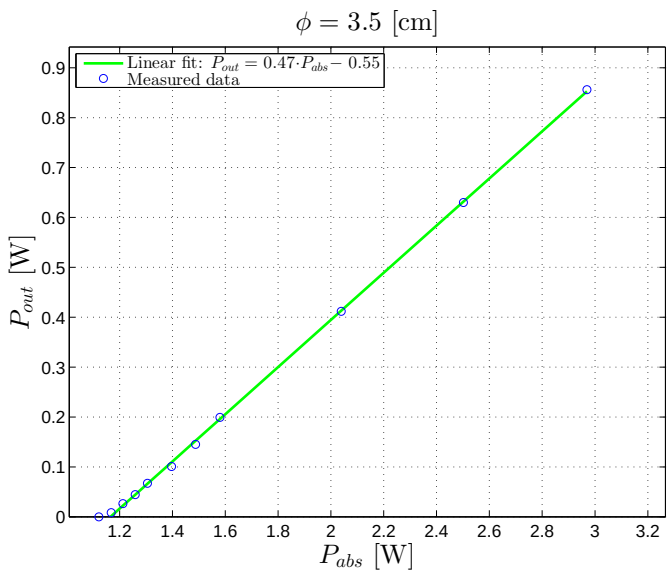

Figure C.8: Output power versus absorbed pump power, at a coiling diameter of 3.5 cm.

Appendix D

Preliminary trials to realize fs-laser inscribed FBGs at 2 μ m

A setup to write FBGs at 2 μm with the PbP-technique for future experiments, with in-house capabilities and more flexibility due to the lack of H-loading, was initiated. However this setup was not considered a priority, and therefore not finished. This appendix talks about how to implement the PbP-technique, with an in-house capability.

FBGs can be fabricated using the PbP-technique, which has been demonstrated in a vast amount of articles, for instance [43] and [44]. This technique utilizes femtosecond pulses with IR light, in this particular case IR at 820 nm, with a repetition rate of 1 kHz. In addition to the pulsed laser, a helium-neon (HeNe) laser was incorporated to simplify the alignment. Figure D.1 shows a schematic over the beam paths and mirror placement. All mirrors are HR at 820 and 632 nm, and are either a metallic or dielectric mirror.

The first optical component the pulsed IR light approaches is a prism, which is used to attenuate the average power. The prism will only reflect about 4% of the incident light, due to Fresnel reflection. The beam continues to mirror M_1 which combines the pulsed beam with the HeNe, and is the only mirror which is not HR at both 632 and 820 nm. M_1 is HR at 820 nm, but highly transmittive (HT) at 632 nm. Thereafter an aperture is placed in the beam path for alignment purposes. Mirror M_2 is a flip mirror, which changes the beam path from an alignment point, to the mirror system M_s. M_s is illustrated in figure D.2, and is a set of mirrors to

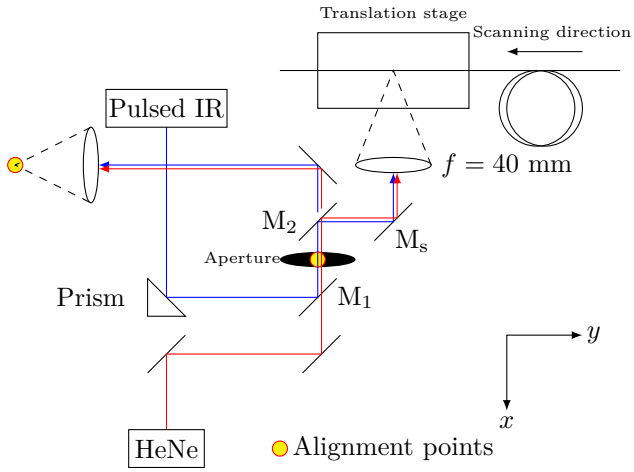

Figure D.1: Sketch of the mirror setup and beam path.

change the height of the beam path. Once the beam has travelled through M_s, a

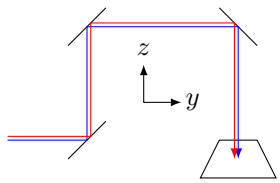

Figure D.2: Illustration of the mirror system in the fiber Bragg grating writing setup. The beam continues in the negative x-direction.

lens with a focal length of 40 mm focuses the beam on the fiber core.

The bare fiber was placed in a custom made fiber holder designed with CAD, and fabricated at KTH, see figure D.3. The fiber holder was in turn mounted on a pitch and yaw platform from Thorlabs (model APY002/M). The scanning was executed by a high precision translation stage, fabricated by Aerotech (model ALS130H-050), with a resolution of $0.5\,\text{nm} - 1\,\mu\text{m}$. Once the fiber was placed in the fiber holder, it had to be precisely aligned. The PbP-technique requires that the fiber core is within the fs-lasers focus during the entire translation. The translation was in the negative y-direction, according to figure D.1. Even though the HeNe-laser was focused on the core, it did not indicate that the IR light is focused. This is due to chromatic dispersion. Since the phase and group velocity of light propagating in

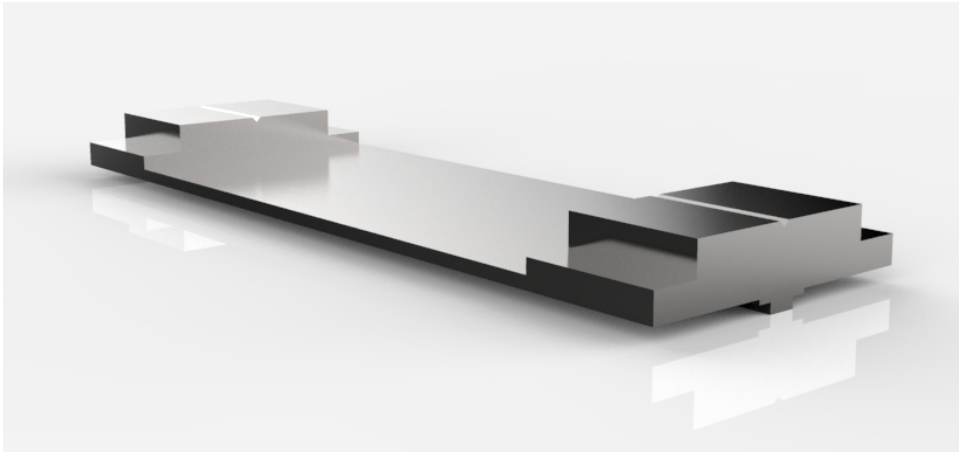

Figure D.3: Virtual prototype of the fiber holder made with a CAD-program.

a fiber (or any medium for that point) depend on the optical frequency, light will have a different refractive index, and hence a different focal length, depending on the light's wavelength. A 40 mm lens was used, and the HeNe-laser aligned to hit the fiber core. When the core was illuminated two diffraction patterns were visible. One dense pattern, from the fiber itself, and one coarse pattern, from the core. A camera from Thorlabs (model DCC1545M) was mounted above the fiber to confirm focusing on the core, see figure D.4.

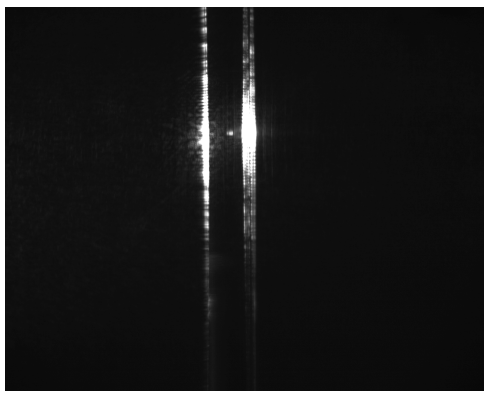

Figure D.4: The camera mounted above the fiber confirming that the infrared light (820 nm) was focused in the core of the passive 1.55 μm-fiber with a core diameter of 10 μm.

In order to adjust the focus point for the IR light, a theoretical approach facilitated the process. The focal length of a lens can be calculated with the lens maker's formula;

$$\frac{1}{f} = (n-1)\left[\frac{1}{R_1} - \frac{1}{R_2} + \frac{(n-1)d}{nR_1R_2}\right], \tag{D.1}$$

where $R_{1,2}$ is the radii of curvature of the lens, with the beam incident to R_1, and d is the thickness of the lens. Since the backside of the lens was flat, $R_2 = \infty$, simplifying (D.1) to

$$\frac{1}{f} = \frac{n-1}{R_1}. \tag{D.2}$$

The refractive index depends on the wavelength according to the Sellmeier equation as

$$n^2(\lambda) = A + \frac{B_1\lambda^2}{\lambda^2 - C_1} + \frac{B_2\lambda^2}{\lambda^2 - C_2}, \tag{D.3}$$

and therefore the focal length depends on the wavelength as well. Assuming that the focal length of 40 mm is accurate for the 632 nm of the HeNe-laser, the focal length at the IR wavelength of 820 nm is about 0.36 mm shorter.

Yet another problem arises when the beam is focused into the core. The fiber itself will act as a lens, and hence shift the position of the focus. According to Geernaert *et al* [45] a low-NA lens will contribute less to this shift due to the fiber curvature. This effect is not negligible, and finding a suitable focal lens using the ABCD law can be advantageous. The following derivation mainly follows the work of Thomas *et al* [46].

Consider a fiber with cladding radius r_{cl}, and assume that the refractive index is uniformly n. Let z and z' be the beam waist position outside and inside the fiber, respectively, where the surface of the fiber is set as the origin. Therefore, when $z' = r_{\mathrm{cl}}$, the focus is within the fiber core.

Now assume a Gaussian beam profile for the laser light and use the paraxial approximation. The complex beam parameter, q and q', can be expressed with the beam parameters waist positions and their corresponding Rayleigh ranges, z_{R} and z'_{R};

$$q = z + \mathrm{i}z_{\mathrm{R}} \text{ and } q' = -z' + \mathrm{i}z'_{\mathrm{R}}. \tag{D.4}$$

According to the paraxial approximation the curved boundary of radius r_{cl} between air and a media of refractive index n is described with the ray-transfer

matrix [11]

$$M = \begin{pmatrix} A & B \\ C & D \end{pmatrix} = \begin{pmatrix} 1 & 0 \\ -\frac{n-1}{nr_{\mathrm{cl}}} & \frac{1}{n} \end{pmatrix}, \tag{D.5}$$

and as Svelto derived in [17] that the ABCD-law for Gaussian beams are

$$q' = \frac{Aq + B}{Cq + D}. \tag{D.6}$$

According to (D.5) $A = 1$ and $B = 0$, which gives the opportunity to separate the real and imaginary part of (D.6). Insert (D.4) in (D.6) and solve for z', which yields

$$z'(z) = \frac{D}{C}\left(\frac{Cz + D}{(Cz + D)^2 + C^2 z_{\mathrm{R}}^2} - \frac{1}{D}\right). \tag{D.7}$$

Remember that z' is the beam waist position inside the fiber, and by altering the lens position in the fiber axis, z can be controlled. As in [46], all length is expressed in units of the fiber cladding radius r_{cl};

$$\tilde{z} = \frac{z}{r_{\mathrm{cl}}} \tilde{z}' = \frac{z'}{r_{\mathrm{cl}}} \tilde{z}_{\mathrm{R}} = \frac{z_{\mathrm{R}}}{r_{\mathrm{cl}}} \text{ and } \tilde{f} = \frac{n}{n-1}, \tag{D.8}$$

where $\tilde{f}$ is the focusing power of lens surface. The beam waist position inside the fiber can now be expressed as

$$\tilde{z}'(\tilde{z}) = -\frac{\tilde{f}}{n}\left(\frac{-\tilde{z}/\tilde{f} + 1/n}{(-\tilde{z}/\tilde{f} + 1/n)^2 + (\tilde{z}_{\mathrm{R}}/\tilde{f})^2} - n\right). \tag{D.9}$$

If the beam waist position outside the fiber is located at $\tilde{z}_{\min} = \tilde{f}/n - \tilde{z}_{\mathrm{R}}$, the beam position inside the fiber, $\tilde{z}'$, reaches its minimum. When this minimum is equal to one, the focal position is located at the fiber core.

$$\tilde{z}'(\tilde{z}_{\min}) = \tilde{f}\left(1 - \frac{\tilde{f}}{2n\tilde{z}_{\mathrm{R}}}\right) = 1 \tag{D.10}$$

Solving (D.10) for z_{R} yields

$$z_{\mathrm{R}} = \frac{nr_{\mathrm{cl}}}{2(n-1)} \tag{D.11}$$

and is thus the ideal Rayleigh range. To relate this ideal z_{R} to a focal length, the ABCD-matrix for a beam focused by a thin lens followed by free-space propagation is used. According to [11] it is

$$\begin{pmatrix} A & B \\ C & D \end{pmatrix} = \begin{pmatrix} 1 - \frac{z}{f} & z \\ -\frac{1}{f} & 1 \end{pmatrix}. \tag{D.12}$$

Now rewrite (D.6) as

$$\frac{1}{q'} = \frac{C + D/q}{A + B/q}, \tag{D.13}$$

where $1/q$ is given by

$$\frac{1}{q} = -\frac{\mathrm{i}\lambda}{\pi w_{01}^2} = -\frac{\mathrm{i}}{z_{\mathrm{R1}}}, \tag{D.14}$$

where z_{R1} corresponds to the Rayleigh range with spot size w_{01} and $1/q'$ is related with z_{R2} and w_{02} in the same manner. If the imaginary parts of (D.13) is set equal, and then solved for w_{02},

$$w_{02} = \frac{\lambda f}{\pi w_{01}\sqrt{1 + \left(\frac{f}{z_{\mathrm{R1}}}\right)^2}} \tag{D.15}$$

is obtained. If the assumption $z_{\mathrm{R1}} \gg f$ is made, the denominator can be reduced and the second beam waist is approximately

$$w_{02} \approx \frac{\lambda f}{\pi w_{01}}. \tag{D.16}$$

The definition of the Rayleigh range is shown in (2.10) and can be interpreted as where the beam width has increased with a factor of $\sqrt{2}$. As (D.11) is the ideal Rayleigh range, it can be set equal to (2.10);

$$z_{\mathrm{R2}} = \frac{\pi}{\lambda} w_{02}^2 = \frac{n r_{\mathrm{cl}}}{2(n-1)}. \tag{D.17}$$

If (D.16) is then substituted into (D.17) and solved for f one arrives at

$$f = \sqrt{\frac{n r_{\mathrm{cl}} \pi w_{01}^2}{2\lambda(n-1)}}. \tag{D.18}$$

The grating periods depend on the repetition rate, r_{r}, and the scanning velocity, v_{s}, as

$$\Lambda = \frac{v_{\mathrm{s}}}{r_{\mathrm{r}}}. \tag{D.19}$$

According to (3.11) the design wavelength depends on the grating period, and by inserting (D.19) in (3.11) a relation between the scanning velocity and the design wavelength can be found;

$$v_{\mathrm{s}} = \frac{\lambda_{\mathrm{D}} r_{\mathrm{r}}}{2 n_{\mathrm{eff}}}. \tag{D.20}$$

In order to write a uniform FBG the core has to be illuminated at a constant scanning velocity. This was realised through the code in Appendix E.

Appendix E

AeroBasic code to control ALS130H-050

```
1  ' Code to write FBGs with the PbP-technique using Aerotech ALS130H-050.
2  ' Set the design wavelength in nm, and the grating length in mm.
3  ' The FBG will be written at a constant velocity.
4  ' By Robert W. Hurra during his Masters thesis project at the Laser Physics dep., KTH 2012-2013
5  ' Title: Narrow Linewidth All-fiber Cavity Thulium Fiber Laser at 2 mu m
6
7  DECLARATIONS
8          GLOBAL lambda_B AS DOUBLE  = 1550        ' Design wavelength [nm]
9          GLOBAL L AS DOUBLE  = 5                  ' Length of grating [mm]
10
11         GLOBAL S_ACC AS DOUBLE = 1               ' Acceleration and deaccelaration distance [mm]
12         GLOBAL r_r AS DOUBLE = 1000              ' Repetition rate [Hz]
13         GLOBAL n_eff AS DOUBLE = 1.445           ' Effective refractive index of the fiber
14         GLOBAL V AS DOUBLE                       ' Velocity of grating writing [mm/s]
15         GLOBAL T_ACC AS DOUBLE                   ' Time of acceleration [s]
16         GLOBAL T_V AS DOUBLE                     ' Time at constant velocity [s]
17         GLOBAL T_TOT AS DOUBLE                   ' Total travelling time [s]
18 END DECLARATIONS
19
20 PROGRAM
21                                                  ' Calculating relevant velocities and times
22         V = lambda_B * r_r / (2 * n_eff) * 10^(-6)
23         T_ACC = 2 * S_ACC / V
24         T_V = L / V
25         T_TOT = T_ACC + T_V
26
27         SCURVE 0
28         ENABLE X Y
29         WAIT MODE MOVEDONE
30         HOME X Y                                 ' Set x- and y-pos to home
31         LINEAR Y -2 F 5                          ' Change y-pos (if a long grating is written,
32                                                  ' adjust properly)
33
```

```
34
35          WAIT MODE NOWAIT
36
37          RAMP MODE DIST
38          RAMP DIST ACCEL S_ACC                ' Set acceleration distance to S_ACC units.
39          RAMP DIST DECEL S_ACC
40
41          LINEAR Y (L+2*S_ACC) F V             ' Move X axis to absolute location of L units,
42                                               ' at V units/sec.
43
44          DWELL T_ACC                          ' Suspend execution during acceleration.
45          PSOCONTROL X ON                      ' Turn the pulses on.
46          DWELL T_V
47          PSOCONTROL X OFF                     ' Turn the pulses off.
48
49          WAIT MODE MOVEDONE
50
51          HOME Y
52          DISABLE X Y
53  END PROGRAM
```